



Effective low-energy RKKY interaction in doped topological crystalline insulatorsMohsen Yarmohammadi ^{*}*Lehrstuhl für Theoretische Physik I, Technische Universität Dortmund, Otto-Hahn Straße 4, 44221 Dortmund, Germany*Hosein Cheraghchi [†]*School of Physics, Damghan University, P.O. Box 36716-41167, Damghan, Iran
and Physics Department, Iran University of Science and Technology, P.O. Box, 16844, Narmak, Tehran, Iran*

(Received 22 May 2020; accepted 16 July 2020; published 5 August 2020)

We study the Ruderman-Kittel-Kasuya-Yosida (RKKY) interaction between two magnetic impurities resided on the (001) plane of topological crystalline insulator (TCI) SnTe associated with four anisotropic Dirac cones protected by the mirror symmetry. The lattice Green's functions governing the correlation of both the sublattices and spins are deduced by developing a two-band effective model. We explore the RKKY Heisenberg interaction of the system established by the interference between four Dirac cones. Our key finding is that, independent of the position of magnetic impurities on the same sublattices or different ones, multiple wave vectors with different orders describe the RKKY coupling physics in TCIs. Further, both the undoped and doped spin susceptibility give rise to the same decay rates like graphene. Magnetic impurities on the same and different sublattices propose the ferromagnetic and antiferromagnetic base phase of the undoped system, respectively. Here we demonstrate that RKKY exchange in TCIs, undergoes a ferromagnetic-to-antiferromagnetic transition and vice versa in response to switching on/off the electron and hole doping. Analytic expressions of doped TCIs are obtained to draw the magnetic phase diagram of the distance between two magnetic impurities and the doping concentration, clarifying the contributions of short and long distances as well as low and high concentrations to the RKKY coupling. Our results may tailor the magnetic features of TCIs for further research and application.

DOI: [10.1103/PhysRevB.102.075411](https://doi.org/10.1103/PhysRevB.102.075411)**I. INTRODUCTION**

Instead of time-reversal symmetry (TRS) in well-known topological insulators (TIs) [1], the surface states of topological crystalline insulators (TCIs) are protected by the crystal symmetry [2]. Although TIs are immune against external perturbations, in TCIs, protection will be failed by any perturbation, which breaks down the crystal symmetry, mirror, or rotational symmetry [3]. The robust surface states of TCIs, at first, theoretically predicted by Hsieh [2] in high-symmetry surfaces of SnTe and related alloys $\text{Pb}_x\text{Sn}_{1-x}$ (Te, Se), and soon after, four Dirac cones were observed in angle-resolved photoemission spectroscopy (ARPES) of the (001) and (111) planes of surface Brillouin zone (SBZ) [4–6]. The low-energy spectrum of SnTe on the (001) plane is based on cation and anion subspace (Te and Sn p orbitals) [3,7]. Dirac points that are located along $X_1\text{-}\Gamma\text{-}X_1$ and $X_2\text{-}\Gamma\text{-}X_2$ lines are not time-reversal invariant. Furthermore, these gapless Dirac cones are sensitive to the symmetry-breaking perturbations such as Zeeman field, ferroelectric-type structural distortion, or strain. Formation of a gap occurs when an out-of-plane magnetic field is applied [2,3]. The fingerprints of perturbations can be also detected in the Landau level spectrum of TCI surface,

which shows an unusual pattern [3]. In three-dimensional (3D) $\text{Cr}(\text{Bi}_{1-y}\text{Sb}_y)_2\text{Te}_3$ thin films, doped magnetic impurities break TRS giving rise to a gap formation, which plays an important role to induce strong ferromagnetism in quantum anomalous Hall insulators [8]. Correspondingly, induced ferromagnetism in SnTe was long known arising from sufficient doped magnetic impurity concentration [9,10] and also in proximity of a ferromagnetic insulator (EuS) [11].

To go through understanding magnetic ordering of TCIs, we study the magnetic response between magnetic impurities substitutionally embedded in the gapped bulk system in the vicinity of the surface, through host itinerant electrons with four Dirac cones spectrum on TCI surfaces. In TCIs, by substitution of magnetic ions in (Sn, Pb), a uniform impurity environment is achievable in a way that there is no bulk magnetic ordering but surface ferromagnetism at low temperatures [3]. One of the straightforward response functions for studying this indirect exchange interaction was derived by Ruderman-Kittel-Kasuya-Yosida (RKKY) [12]. The RKKY interaction interprets long-range and oscillating behavior of spin-spin exchange interaction. The RKKY coupling usually decays as R^{-2} for the 2D conventional electron gas [13], while for Dirac materials, it decays faster in short-distances of magnetic impurities [14,15]. In degenerated systems such as graphene, an isotropic and colinear coupling is dominant, which is called Heisenberg interaction [14]. However, in TIs, as a conclusion of strong Rashba spin-orbit

^{*}mohsen.yarmohammadi@tu-dortmund.de[†]cheraghchi@du.ac.ir

interaction, Dirac spinors of the chiral edge states include spin-momentum locking, which could result in Ising-like term (anisotropic but collinear interaction), Dzyaloshinskii-Moria like term (anisotropic and noncollinear interaction), and even more complicated interactions [16]. Topological semimetals such as three-dimensional Weyl/Dirac semimetals are also the frontier field of the topological materials. In the works by Chang *et al.* and Hosseini *et al.* [17–20], the RKKY interaction between magnetic impurities in both Dirac and Weyl semimetals have been theoretically studied to explore the effects of anisotropic band dispersion and also its unique 3D spin momentum on the RKKY response including the Heisenberg, the Ising, and the Dzyaloshinsky-Moriya terms, which lead to fascinating spin textures and possible ferromagnetism in these materials. Moreover, they have found that for each term the decaying rate of RKKY interaction obeys the power law of R^{-5} , demonstrating the beating behavior depending on the impurities' orientations. Oscillation pattern in RKKY interaction depends on the interference of the Fermi wave vectors of host itinerant electrons involving in indirect exchange interaction. For example, in graphene Fermi momentum and also $K - K'$ controls oscillatory factor [14]. Regarding the diversity of Fermi wave vectors and also anisotropic Dirac cones in SBZ of TCIs, unusual features are expected, which would be different from other Dirac materials. In comparison, Weyl semimetals have two split nodal points in the Brillouin zone, which the internode processes leads to an additional oscillatory pattern in RKKY interaction [17,18].

In this work, we investigate RKKY exchange interaction between two magnetic impurities resided in TCIs mediated by host anisotropic Dirac fermions on the (001) SBZ. At first, we developed two-band effective Hamiltonian to extract spectrum beyond the four Dirac cones, which are usually considered for the low-energy spectrum. Then, by calculating lattice Green's function, susceptibility, which is related to the RKKY exchange coupling is analytically analyzed in pristine and doped TCIs. The interference part of susceptibility indicates strong anisotropy of TCIs in terms of the direction of two magnetic impurities on the (001) surface, which is periodic when impurities are located on the same or different sublattices. A beating-type oscillation seen in RKKY exchange coupling is originated from the interference of wave functions attributed to each Fermi wave vectors. In the doped TCI, we present a phase diagram showing that the ferromagnetic-to-antiferromagnetic phase transition occurs asymmetrically for the electron- or hole-doped TCI. Indeed, we show that the electron-hole symmetry will be revived for susceptibility at large enough distances between two magnetic impurities or strong enough doping.

The presentation of the paper contains the following sections. In Sec. II, four-band Hamiltonian and its general features are reviewed and then Green's function in SBZ and the density of states are presented in Sec. III. The RKKY mechanism is reviewed in Sec. IV, which will be completed by formula required to calculate the lattice Green's function. In Sec. V, we derive a two-band model at low energy, which is the background for calculating RKKY exchange interaction for pristine TCIs in Sec. VA and doped TCI in Sec. VB. Finally, we discuss the outlook of the results in Sec. VI and conclude the paper in Sec. VII.

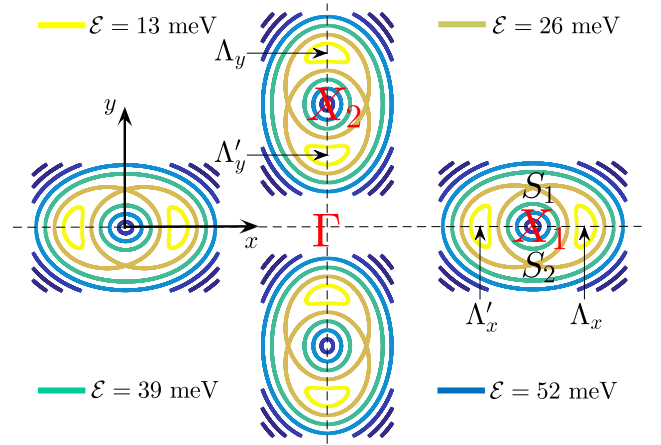


FIG. 1. Bounded (centered) SBZ by the X_1/X_2 (Γ) point. Low-energy Dirac cones, i.e., metallic gapless SnTe (001) surface states, are located at $\{\Lambda_x, \Lambda'_x\}$ and $\{\Lambda_y, \Lambda'_y\}$ points near the X_1 and X_2 point, respectively. Two disconnected electron pockets suffer from a Lifshitz transition at energies $\mathcal{E} = \pm\delta$, emerging two saddle points S_1 and S_2 (e.g., see around X_1 point).

II. THEORETICAL BACKGROUND

We begin by representing the Hamiltonian of the SnTe (001) surface states as well as related alloys [21], setting the physical constant $\hbar = 1$ for simplicity throughout the paper. To confirm the experimental observations of these states using the ARPES method [2,4,6,22–25], a representation particularly useful for low-dimensional systems is the $\vec{k} \cdot \vec{p}$ description, leading to the following clean Hamiltonian near both X_1 and X_2 points of the SBZ [4,22,23,26–36]:

$$\hat{\mathcal{H}}_{X_1}(\vec{k}) = \eta_1 k_x \hat{\sigma}_y - \eta_2 k_y \hat{\sigma}_x + n \hat{\tau}_x + \delta \hat{\sigma}_y \hat{\tau}_y, \quad (1a)$$

$$\hat{\mathcal{H}}_{X_2}(\vec{k}) = \eta_2 k_x \hat{\sigma}_y - \eta_1 k_y \hat{\sigma}_x + n \hat{\tau}_x + \delta \hat{\sigma}_x \hat{\tau}_y, \quad (1b)$$

where $\eta_1 = 1.3 \text{ eV \AA}$ and $\eta_2 = 2.4 \text{ eV \AA}$ are typical Fermi velocities obtained from numerical *ab initio* calculations [2,24,37]. While $\hat{\sigma} = (\hat{\sigma}_x, \hat{\sigma}_y)$ are the Pauli matrices for two spin components, so-called Kramers' doublet, the Pauli matrices for describing the cation-anion degree of freedom are given by $\hat{\tau} = (\hat{\tau}_x, \hat{\tau}_y)$. As for the intervalley scattering at the lattice scale, two parameters $n = 70 \text{ meV}$ and $\delta = 26 \text{ meV}$ are introduced having only three allowed symmetry operators $\hat{\tau}_x$, $\hat{\sigma}_x \hat{\tau}_y$ and $\hat{\sigma}_y \hat{\tau}_y$ up to zeroth-order momenta $\vec{k} = (k_x, k_y)$ [2]. These Hamiltonians are understood as follows. Let us assume $n = 0$ and $\delta = 0$. Two Dirac cones in the conduction and valence bands touch each other at the zero energy. Switching on n shifts these touched Dirac cones to intersect one another, forming an intersection elliptic. Also, switching on δ leads to turning the level crossing into the level anticrossing, where Dirac cones emerge at two separate points

From Eqs. (1a) and (1b), the transformation of $\hat{\mathcal{H}}_{X_1}(\vec{k}) \leftrightarrow \hat{\mathcal{H}}_{X_2}(\vec{k})$ is evident due to fourfold C_4 discrete rotation symmetry described by $\hat{\sigma}_x \mapsto \hat{\sigma}_y$, $\hat{\sigma}_y \mapsto -\hat{\sigma}_x$, $k_x \mapsto k_y$, and $k_y \mapsto -k_x$. From this point, we will focus on the dynamics near one of the X_1 and X_2 points only in what follows. Thereby, the Dirac energy-momentum dispersions for four gapless states

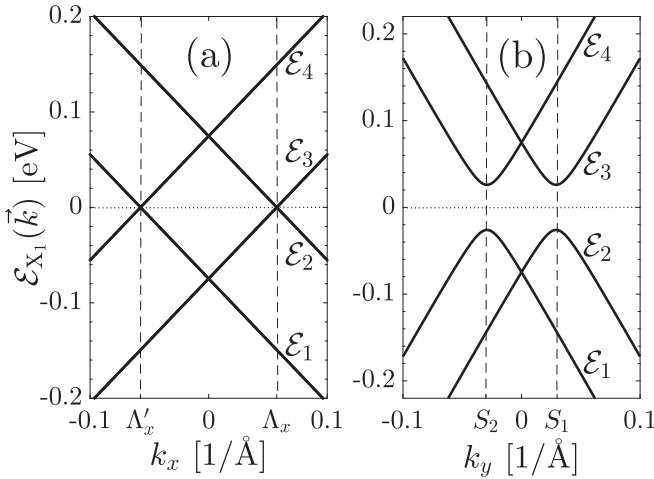


FIG. 2. The electronic dispersion energy of Dirac fermions near the X_1 point of the SBZ at (a) $k_y = 0$ and (b) $k_x = 0$.

near X_1 point can be easily obtained via diagonalizing the Hamiltonian in Eq. (1a), given by

$$\mathcal{E}_{X_1}^{\mu,\nu}(\vec{k}) = \mu\sqrt{f(\vec{k})} + \nu g(\vec{k}), \quad (2a)$$

$$f(\vec{k}) = n^2 + \delta^2 + \eta_1^2 k_x^2 + \eta_2^2 k_y^2, \quad (2b)$$

$$g(\vec{k}) = 2\sqrt{(n^2 + \delta^2)\eta_1^2 k_x^2 + n^2 \eta_2^2 k_y^2}, \quad (2c)$$

where $\mu = +(-)$ and $\nu = +(-)$ stand for the conduction (valence) band and Λ_x (Λ'_x) Dirac point, respectively (see Figs. 1 and 2 for more details). From the above equation, one obtains direction-dependent branches dispersing from $\vec{k} = 0$ to $\vec{k} \neq 0$. In the case of both $k_x = 0$ and $k_y = 0$, two Dirac cones emerge at energies $\mathcal{E} = \pm\sqrt{n^2 + \delta^2}$ and at $\mathcal{E} = 0$, two Dirac cones take place at the momenta $\Lambda_x = (+\sqrt{n^2 + \delta^2}/\eta_1, 0)$ and $\Lambda'_x = (-\sqrt{n^2 + \delta^2}/\eta_1, 0)$ with $k_y = 0$, referring to the metallic gapless SnTe (001) surface states.

In addition, for the \vec{k} point with $k_x = 0$, one achieves two saddle points $S_1 = (0, +n/\eta_2)$ and $S_2 = (0, -n/\eta_2)$ along the y direction at which two disconnected electron pockets at low-energy Dirac cones suffer from a Lifshitz transition at energy $\mathcal{E} = \pm\delta = \pm 26$ meV [2,22], as represented in Fig. 1. Figure 1 shows that the SBZ is centered at the Γ point, while it is bounded to the X_1 and X_2 points. Moreover, the Dirac cones reside at the mirror symmetry invariant points slightly away from the X_1 and X_2 points, meaning that the topologically protected symmetry in SnTe (001) surface is the mirror symmetry, not time-reversal symmetry. With the aid of such a contour plot, we understand there is an anisotropic property for fermion pockets around each of X_1 and X_2 points, implying that the spatial fermionic wave functions are not distributed similarly around these points, leading to different physics. While some authors may investigate the whole \vec{k} -points effects obtained by considering the quantum nature of the system, for quantum spectral intensities we treat the SBZ high-symmetry lines as an individual. Particularly, we intend to show the band structures for different momenta. It is necessary to briefly mention that to derive the energy

dispersion around X_2 point, replacement $k_y \mapsto k_x$ in Eqs. (2b) and (2c) is adequate.

As shown in Fig. 2, we consider a situation in which the momenta \vec{k} are set by the coordinates of the SBZ. For the case of $k_y = 0$, we deal with linear dispersion energy dependent on k_x only, which exemplifies the textbook case of the graphene-like equations. As explained before, two gapless surface states take place at two Λ_x and Λ'_x points [Fig. 2(a)] with energies zero, while two more Dirac points would like to emerge at $k_x = k_y = 0$ with nonzero energies. For the case of $k_y = 0$, quadratic curves occur at two saddle points S_1 and S_2 [Fig. 2(b)]. Simply, it is expected to have those nonzero Dirac bands at $k_y = k_x = 0$ as well.

III. RECIPROCAL-SPACE GREEN'S FUNCTIONS AND ELECTRONIC DENSITY OF STATES

Although the correlation between fermionic wave functions can be simply described in various ways, we use the Green's function approach to do so for simplicity because the band dispersion of the system manifests itself in the Green's function poles [38,39]. The noninteracting Green's function matrix in the \vec{k} space is obtained through the relation $\hat{G}^0(\vec{k}, \mathcal{E}) = 1/[\mathcal{E} + io^+ - \mathcal{H}_{X_1}(\vec{k})]$, where $o^+ = 5$ meV is the phenomenological/numerical broadening factor. By this, one obtains (in the basis set of $\{|c, \uparrow\rangle, |a, \uparrow\rangle, |c, \downarrow\rangle, |a, \downarrow\rangle\}$)

$$\underline{\underline{G}}^0(\vec{k}, \mathcal{E}) = \begin{pmatrix} G_{cc}^{\uparrow\uparrow} & G_{ca}^{\uparrow\uparrow} & G_{cc}^{\uparrow\downarrow} & G_{ca}^{\uparrow\downarrow} \\ G_{ac}^{\uparrow\uparrow} & G_{aa}^{\uparrow\uparrow} & G_{ac}^{\uparrow\downarrow} & G_{aa}^{\uparrow\downarrow} \\ G_{cc}^{\downarrow\uparrow} & G_{ca}^{\downarrow\uparrow} & G_{cc}^{\downarrow\downarrow} & G_{ca}^{\downarrow\downarrow} \\ G_{ac}^{\downarrow\uparrow} & G_{aa}^{\downarrow\uparrow} & G_{ac}^{\downarrow\downarrow} & G_{aa}^{\downarrow\downarrow} \end{pmatrix}, \quad (3)$$

where all elements are \vec{k} and \mathcal{E} dependent. Also, c (a) and \uparrow (\downarrow) refer to the cation (anion) sublattice and the spin up (down), respectively. Some elements are the same in general due to the crystal lattice symmetries. Depending on the purpose of the physical quantity under study, elements come to play important roles. For example, for the partial, local, and total density of states, the most contribution of correlations is important, which comes from the diagonal elements. We start with the diagonal elements

$$G_{cc}^{\uparrow\uparrow} = G_{aa}^{\downarrow\downarrow} = \frac{a_D}{\tilde{\mathcal{E}} - \mathcal{E}_1} + \frac{b_D}{\tilde{\mathcal{E}} - \mathcal{E}_2} + \frac{c_D}{\tilde{\mathcal{E}} - \mathcal{E}_3} + \frac{d_D}{\tilde{\mathcal{E}} - \mathcal{E}_4}, \quad (4a)$$

$$G_{cc}^{\downarrow\downarrow} = G_{aa}^{\uparrow\uparrow} = \frac{d_D}{\tilde{\mathcal{E}} - \mathcal{E}_1} + \frac{c_D}{\tilde{\mathcal{E}} - \mathcal{E}_2} + \frac{b_D}{\tilde{\mathcal{E}} - \mathcal{E}_3} + \frac{a_D}{\tilde{\mathcal{E}} - \mathcal{E}_4}, \quad (4b)$$

where $\tilde{\mathcal{E}} = \mathcal{E} + io^+$ and (see Fig. 1)

$$\mathcal{E}_1 = -\sqrt{f(\vec{k}) + g(\vec{k})}, \quad \mathcal{E}_2 = -\sqrt{f(\vec{k}) - g(\vec{k})}, \quad (5a)$$

$$\mathcal{E}_3 = +\sqrt{f(\vec{k}) - g(\vec{k})}, \quad \mathcal{E}_4 = +\sqrt{f(\vec{k}) + g(\vec{k})}, \quad (5b)$$

$$a_D = \frac{1}{4} \left(1 + 2 \frac{n\delta\eta_2 k_y}{g(\vec{k})\mathcal{E}_1} \right), \quad b_D = \frac{1}{4} \left(1 - 2 \frac{n\delta\eta_2 k_y}{g(\vec{k})\mathcal{E}_2} \right), \quad (5c)$$

$$c_D = \frac{1}{4} \left(1 - 2 \frac{n\delta\eta_2 k_y}{g(\vec{k})\mathcal{E}_3} \right), \quad d_D = \frac{1}{4} \left(1 + 2 \frac{n\delta\eta_2 k_y}{g(\vec{k})\mathcal{E}_4} \right). \quad (5d)$$

Since the density of states is proportional to the Green's function (see the next paragraph), the weight coefficients refer

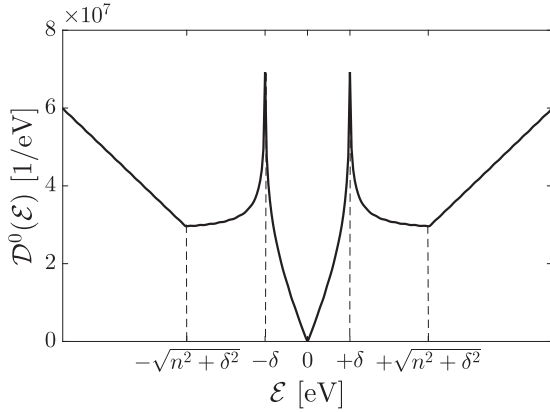


FIG. 3. Total clean DOS of the SnTe (001) surface. Two important energies $\pm\sqrt{n^2 + \delta^2}$ and $\pm\delta$, one Van Hove singularity, and one nick, respectively, are labeled at each conduction and valence band.

to the contribution of each basis set in the band spectrum. In other words, the weight coefficients (a_D , b_D , c_D , and d_D) presented in Eq. (5), are attributed to the partial density of states along the SBZ.

We note that the only terms generated compared to two copies of \vec{k} -space Green's functions in graphene are those intervalley scattering parameters n and δ . The conventional approach is to symmetrize the correlations to obtain new simplified Green's functions. However, this is easy to do so for the diagonal Green's functions, but this is not the case for off-diagonal elements and one needs to perform more calculations depending on the purpose. Because of the high number of fermionic states in both conduction or valence bands, the density of states (DOS) may help to catch the electronic features of the system. The total clean DOS is obtained by summing over the whole SBZ through $\mathcal{D}^0(\mathcal{E}) = -(1/\pi) \sum_{\vec{k} \in \text{SBZ}} \text{Im} [\text{Tr} \underline{G}^0(\vec{k}, \mathcal{E})]$, leading to

$$\mathcal{D}^0(\mathcal{E}) = -\frac{2}{\pi} \text{Im} \left[\tilde{\mathcal{E}} \left(\frac{1}{\tilde{\mathcal{E}}^2 - \mathcal{E}_1^2} + \frac{1}{\tilde{\mathcal{E}}^2 - \mathcal{E}_2^2} \right) \right], \quad (6)$$

originating from this fact that for all \vec{k} points, $a_D + b_D = c_D + d_D = \frac{1}{2}$ in Eqs. (5c) and (5d). Looking at these equations, it is obvious that $a_D + b_D$ and $c_D + d_D$ does not depend on the choice of X_1 and X_2 points. Indeed, since the band spectrum on each X_1 and X_2 point in the SBZ is the same (except a $\pi/2$ rotation), calculation of DOS around each of these points in \vec{k} summation leads to similar results. However, as it will be shown in the next section, for calculating real-space Green's functions and as a consequence, RKKY couplings, we need to consider both of these two specific points in SBZ, since they play crucial roles in quantum interference between magnetic impurities.

Following the calculations above, DOS of Dirac fermions on the SnTe (001) surface is printed in Fig. 3. As expected, the SnTe (001) surface states consist of symmetric Dirac cones. The corresponding DOS of surfaces for energies $|\mathcal{E}| < \delta$ are two linear curves. By increasing the Fermi energy from the Dirac points, at energy $|\mathcal{E}| = \delta$, a Van Hove singularity appears, corresponding to the Lifshitz transition point, i.e., the point that the topology of the Fermi surface alters at

this energy point, those above-described saddle points S_1 and S_2 form. Eventually, once the Fermi energy becomes larger than the δ value ($|\mathcal{E}| > \delta$), DOS decreases up to the time-reversal protected crossed bands at X_1 point with energies $|\mathcal{E}| = \sqrt{n^2 + \delta^2}$, since two separated centered wave pockets are formed (see Fig. 1). Afterward, the fermions disperse to greater energies with an increasing trend for indicating second Dirac cones is being contributed to DOS. The present DOS plotted here is in quite an agreement with Refs. [2,24,40].

IV. RKKY INTERACTION

Let us consider two localized impurities possessing magnetic moments of \mathbf{S}_1 and \mathbf{S}_2 , which are embedded inside the SnTe (001) surface and related alloys at positions \mathbf{R}_1 and \mathbf{R}_2 , respectively. They interact with each other indirectly mediated by itinerant electrons in the conduction band of the system. The interacting Hamiltonian is given by

$$\mathcal{H}_{\text{int}} = J_c \sum_{l=1,2} \delta(\mathbf{r} - \mathbf{R}_l) \mathbf{S}_l \cdot \hat{\mathbf{s}}(\mathbf{r}), \quad (7)$$

where J_c is the exchange coupling between the l th magnetic moment \mathbf{S}_l of the impurity located at \mathbf{R}_l and the spin of conduction electrons $\hat{\mathbf{s}} = \frac{\hbar}{2} \hat{\sigma}$ located at \mathbf{r} . In weak exchange coupling, it is straightforward to use the second-order perturbation theory to derive RKKY Hamiltonian as follows:

$$\mathcal{H}_{\text{RKKY}}^{\gamma\zeta} = J_c^2 \sum_{i,j} S_1^{i\gamma} \chi_{ij}^{\gamma\zeta}(\mathbf{R}, \mathbf{R}') S_2^{j\zeta}, \quad (8)$$

where indices γ (ζ) refers to the cation (anion) sublattice and $i, j \in \{x, y, z\}$ determine the direction of magnetic moment of l th localized impurity. On the other hand, the spin susceptibility tensor in real space can be read as

$$\chi_{ij}^{\gamma\zeta}(\mathbf{R}, \mathbf{R}') = -\frac{1}{2\pi} \text{Im} \int_{-\infty}^{\mathcal{E}_F} d\mathcal{E} \mathcal{E} \mathcal{C}_{ij}^{\gamma\zeta}(\mathcal{E}, \mathbf{R}, \mathbf{R}'), \quad (9)$$

where

$$\mathcal{C}_{ij}^{\gamma\zeta}(\mathcal{E}, \mathbf{R}, \mathbf{R}') = \text{Tr} [\sigma_i G_{\gamma\zeta}^0(\mathcal{E}, \mathbf{R}, \mathbf{R}') \sigma_j G_{\zeta\gamma}^0(\mathcal{E}, \mathbf{R}', \mathbf{R})], \quad (10)$$

and $G_{\gamma\zeta}^0(\mathcal{E}, \mathbf{R}, \mathbf{R}')$ is the real-space noninteracting Green's function, which is a 2×2 matrix in spin space.

We proceed our calculations of the RKKY coupling by commenting on the possibility of the existence of the exchange field as the consequence of doped magnetic impurities, where the gap may emerge in the system. In general, the exchange field is a property of the magnetic impurity inducing to the system as a pseudomagnetic field and opens a gap in the band structure. However, this would require an extension of the model to a nonlinear model to accommodate extra features [7,41,42]. Here, we only consider the magnetic moment of the impurities and neglect the effect of their inherent exchange field. Thereby, there is no gap injection from the exchange field induced by magnetic impurities and the linear contribution of the spin susceptibility is included in the following only.

Let us derive the real-space Green's functions mentioned above. To this end, the lattice Green's function of conduction electrons in real space could be extracted by taking the Fourier transformation of the \vec{k} -space Green's functions around two

in-equivalent X_1 and X_2 points in the SBZ [14,43,44]. Thereby,

$$G_{\gamma\zeta}^0(\mathcal{E}, \mathbf{R}, 0) = \frac{1}{\Omega_{\text{SBZ}}} \int d^2q e^{i\vec{q}\cdot\mathbf{R}} \left[e^{i\vec{X}_1\cdot\mathbf{R}} G_{\gamma\zeta}^0(\vec{q} + \vec{X}_1, \mathcal{E}) + e^{i\vec{X}_2\cdot\mathbf{R}} G_{\gamma\zeta}^0(\vec{q} + \vec{X}_2, \mathcal{E}) \right], \quad (11)$$

where the wave vector \vec{q} is measured closely from the variations around X_1 and X_2 points, i.e., $|\vec{q}| \ll |\vec{X}_1|, |\vec{X}_2|$. The Green's function only depends on distance $(\mathbf{R} - \mathbf{R}')$ between impurities, not to the position of each impurity, \mathbf{R} and \mathbf{R}' . For this reason, we would set one of the magnetic impurities located at \mathbf{R}' to zero. This gives rise to the distance between them \mathbf{R} only. This, in turn, means that $G_{\gamma\zeta}^0(\mathcal{E}, \mathbf{R}, 0) = G_{\gamma\zeta}^0(\mathcal{E}, 0, \mathbf{R})$. To calculate the Green's function, we could get help from the 2D polar coordination (q, ϕ_q) , for which $d^2q = q dq d\phi_q$. On the other hand, one is allowed to rewrite $\exp[i\vec{q}\cdot\mathbf{R}] = \exp[iqR \cos(\phi_q - \phi_R)]$. Here polar angles are measured from distance vector as $\phi_R = \tan^{-1}(R_y/R_x)$ and from wave vector as $\phi_q = \tan^{-1}(q_y/q_x)$. Let us rewrite the integral in Eq. (11) as

$$G_{\gamma\zeta}^0(\mathcal{E}, \mathbf{R}, 0) = \sum_{l=1,2} e^{i\vec{X}_l\cdot\mathbf{R}} G_{\gamma\zeta}^{0,X_l}(\mathcal{E}, \mathbf{R}, \phi_R), \quad (12)$$

wherein

$$G_{\gamma\zeta}^{0,X_l}(\mathcal{E}, \mathbf{R}, \phi_R) = \frac{1}{\Omega_{\text{SBZ}}} \int_0^{q_c} q dq \int_0^{2\pi} d\phi_q e^{iqR \cos(\phi_q - \phi_R)} G_{\gamma\zeta}^{0,X_l}(\mathcal{E}, \vec{q} + \vec{X}_l, \phi_q). \quad (13)$$

In the above equation, q_c is the cutoff wave vector, which is determined by convergence of different physical properties, e.g., DOS. It should be pointed out that the energy correspondence of the cutoff wave vector must not interfere inside the bulk spectrum. Unfortunately, in the Hamiltonian $\hat{\mathcal{H}}_{X_1, X_2}(\vec{k})$, Fermi velocities η_1 and η_2 in x and y directions are different, giving rise to ϕ_q dependence of the Green's functions. So its analytical calculations would be probably too difficult and we must go through numerical calculations.

In what follows, we simplify the original theory of Dirac fermions on the SnTe (001) surface, which helps to find analytical solutions. In the band structure of the SnTe (001) surface, high-energy scales are well separated from the low-energy sector situated around the Fermi energy. Therefore, low-energy Hamiltonians can be constructed having the advantage of being formulated in a smaller Hilbert space. The price for this simplification is often that both the Hamiltonian and the operators take a form that is not more complicated than that of the original theory. In our system, an important role is played by the intervalley scattering, and suitable methods keeping n and δ that go beyond the original theory have to be adopted.

V. EFFECTIVE LOW-ENERGY 2×2 HAMILTONIAN

In this section, we derive the two-band Hamiltonian for very low-energy electronic excitations of surface states projected on (001) surface of SBZ. By applying the suitable basis transformation and expanding the Bloch Hamiltonian in the series of the momentum measured from a Dirac point, the low-energy Hamiltonian of the system can be explicitly an-

alytically derived and proved to be a Dirac-like Hamiltonian. This effective Hamiltonian contains all symmetries as well as Dirac points located at $(\Lambda_x, \Lambda'_x, \Lambda_y, \Lambda'_y)$, which is valid for two energy regions: (i) the first one would be for energies lower than the Lifshitz transition point $|\mathcal{E}| \leq \delta$ and (ii) the region for $\delta \leq |\mathcal{E}| \leq \sqrt{n^2 + \delta^2}$.

In fact, 4×4 Hamiltonian describes high-energy bands emerging around secondary Dirac cones at energies $|\mathcal{E}| \geq \sqrt{n^2 + \delta^2}$. These secondary Dirac cones are appearing on the valleys X_1 and X_2 points. This implies that by linearizing the band structure around the Dirac points, i.e., near the Fermi level, the Hamiltonian presented in Eq. (1a) can be rewritten in the following basis set of cation and anions ($|c \uparrow\rangle, |a \uparrow\rangle, |c \downarrow\rangle, |a \downarrow\rangle$):

$$\underline{\mathcal{H}}_{X_1}(\vec{k}) = \begin{pmatrix} 0 & n & -\Pi & -\delta \\ n & 0 & \delta & -\Pi \\ -\Pi^\dagger & \delta & 0 & n \\ -\delta & -\Pi^\dagger & n & 0 \end{pmatrix}, \quad (14)$$

where $\Pi = i\eta_1 k_x + \eta_2 k_y$. We divide this Hamiltonian into four blocks each of them is a 2×2 matrix; two diagonal blocks, $h_{11} = h_{22} = n\tau_x$ and two off-diagonal blocks $h_{12} = \begin{pmatrix} -\Pi & -\delta \\ \delta & -\Pi \end{pmatrix}$, $h_{21} = h_{12}^\dagger$.

Very low-energy states of electrons are the contribution of wave functions localized on the cations and anions. So the best basis set in which effective 2×2 Hamiltonian can be written would be ($|c \uparrow\rangle, |a \uparrow\rangle$). Furthermore, the parameter n , which corresponds to the interaction between cation and anions is a dominant parameter considered as an unperturbed part of Hamiltonian. The dominant contribution of n in the intervalley process can be understood from its responsibility for the band inversion as a result of the spin-orbit coupling. As a result of this, we divide Hilbert space into two parts of states:

$$|1\rangle := (|c \uparrow\rangle, |a \uparrow\rangle), \quad |2\rangle := (|c \downarrow\rangle, |a \downarrow\rangle). \quad (15)$$

Now we ask to evaluate Green's function projected on the states $|1\rangle$ defining the Green's function as

$$\underline{\underline{G}}(\vec{k}, \mathcal{E}) = \begin{pmatrix} G_{11} & G_{12} \\ G_{21} & G_{22} \end{pmatrix} = \begin{pmatrix} (G_{11}^0)^{-1} & -h_{12} \\ -h_{21} & (G_{22}^0)^{-1} \end{pmatrix}^{-1}, \quad (16)$$

where $G_{ii}^0 = (\tilde{\mathcal{E}} - h_{ii})^{-1}$. The component of G_{11} is related to the perturbed effective Hamiltonian as, $h_{11}^{\text{eff}} = \tilde{\mathcal{E}} - G_{11}^{-1}$ (due to the mostly contribution of n to the intervalley scattering process). So we can use of the above bipartite partitioning technique [45–47] and write

$$G_{11} = G_{11}^0 [1 - G_{11}^0 h_{12} G_{22}^0 h_{21}]^{-1}. \quad (17)$$

Thereby one can derive effective Hamiltonian projected on the states $|1\rangle$ through

$$h_{11}^{\text{eff}} = h_{11} + h_{12} G_{22}^0 h_{21}, \quad (18)$$

where $G_{22}^0 = (\tilde{\mathcal{E}} - n\hat{\tau}_x)^{-1}$. We note that the contribution of both spin up and spin down for which the system reaches the same physics appears in the correlation given by the second term to be near the original theory. This implies that beyond the four-band theory and within the two-band method, the physics of the system does not melt and can longer be

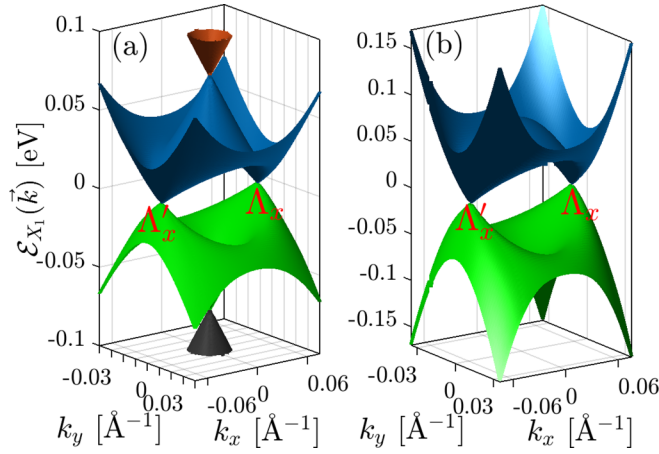


FIG. 4. 3D energy spectrum of TCI SnTe projected on SBZ (001) as functions of k_x and k_y around X_1 point, extracted by (a) 4×4 Hamiltonian and (b) effective 2×2 Hamiltonian.

considered as it is. In the low-energy limit $|\mathcal{E}| \ll n$, one can expand G_{22}^0 in terms of n^{-1} . To this end, we unveil 2×2 effective Hamiltonian around the valley X_1 located on the surface SnTe(001) of SBZ as the following:

$$\hat{h}_{X_1}^{\text{eff.}}(\vec{k}) = \frac{1}{n}[(n^2 + \delta^2 - \Pi^\dagger \Pi)\hat{\tau}_x - 2\delta\eta_2 k_y \hat{\tau}_z]. \quad (19)$$

Consequently, the valid very low-energy band spectrum for energy range of $0 \leq \mathcal{E} \leq \sqrt{n^2 + \delta^2}$ is given by

$$\mathcal{E}_{X_1}^{\text{eff.}}(\vec{k}) = \mu \sqrt{\mathcal{P}^2(k_x, k_y) + \mathcal{Q}^2(k_y)}, \quad (20a)$$

$$\mathcal{P}(k_x, k_y) = \frac{n^2 + \delta^2 - \eta_1^2 k_x^2 - \eta_2^2 k_y^2}{n}, \quad (20b)$$

$$\mathcal{Q}(k_y) = \frac{2\delta\eta_2 k_y}{n}. \quad (20c)$$

It is evident that n and δ appears in the zero-order approximation, so-called continuum limit, and every band inversion in the bulk generates a massless Dirac fermion on the surface at the location that is projecting the momentum on to the surface. The hybridized Dirac points are generated by the intervalley scattering processes characterized by the modified n - and δ -dependent \mathcal{P} and \mathcal{Q} . These intervalley scattering parameters change the low-energy properties a lot but preserve the high-energy properties. Momentum-energy dispersions of SnTe (001) double-Dirac-cone surface states around X_1 point of the SBZ is presented in Fig. 4. The Dirac cones are located at Λ_x and Λ'_x in both models. Figure 4(a) displays the bands spectrum derived by full 4×4 Hamiltonian of Eq. (20) in compared to the spectrum of 2×2 effective Hamiltonian presented in Eq. (1a). This is a unified approach to study Dirac topological surface states and as it is seen, the whole low-energy feature of the original spectrum can be covered by the effective Hamiltonian.

Let us go back to the real-space Green's functions calculations. To do so, we first calculate the effective reciprocal-space Green's functions. Indeed, significant physics of linear spin susceptibility in (001) direction of SnTe is mostly originated from electron states of four Dirac cones. As a result of this

fact, the phase shift of electron states on Dirac cones excited by localized magnetic impurities concludes constructive and destructive interference of wave functions giving rise to an oscillatory behavior of RKKY interactions. Therefore, we will achieve the fundamental behavior of RKKY interaction if we go much closer to the Dirac cones. For the valley X_1 , let us assume that $\eta_2 k_y \ll \eta_1 k_x$, which is equivalent to the energies less than $\eta_2 k_y \ll \sqrt{n^2 + \delta^2}$ for $k_x \approx \Lambda_x$ [4–6]. By usage of this approximation, the function \mathcal{P} in the effective band spectrum would be simplified around $k_x = +\Lambda_x$ as

$$\tilde{\mathcal{P}}|_{k_x \approx +\Lambda_x} \approx \frac{n^2 + \delta^2 - \eta_1^2 k_x^2}{n} = -\frac{2\eta_1^2 \Lambda_x}{n} \tilde{k}_x, \quad (21)$$

where $\tilde{k}_x = k_x - \Lambda_x$. So the effective Hamiltonian shown in Eq. (19) is readily written close to the anisotropic Dirac cones centered at the points $k_x = +\Lambda_x$ in the SBZ,

$$\hat{h}_{\Lambda_x}^{\text{eff.}}(\vec{k}) = -\xi_1 \tilde{k}_x \hat{\tau}_x - \xi_2 k_y \hat{\tau}_z, \quad (22)$$

where the Fermi velocity along x and y direction is defined as $\xi_1 = (2\sqrt{n^2 + \delta^2}/n)\eta_1$ and $\xi_2 = (2\delta/n)\eta_2$, respectively. The wave vector k_y is measured from k_x axis, so we have $\tilde{k}_y = k_y$. The above Hamiltonian can be further simplified as

$$\hat{h}_{\Lambda_x}^{\text{eff.}}(\vec{q}) = v_F[-\tilde{q}_x \hat{\tau}_x - \tilde{q}_y \hat{\tau}_z], \quad (23)$$

where the unified Fermi velocity is given by $v_F = \sqrt{\xi_1 \xi_2}$ and the new wave vector operators are defined as $\tilde{q}_x = \sqrt{\xi_1/\xi_2} \tilde{k}_x$ and $\tilde{q}_y = \sqrt{\xi_2/\xi_1} \tilde{k}_y$. Thus, the effective band spectrum of the anisotropic Dirac cones along the Γ - X_1 direction reads as

$$\mathcal{E}_{\Lambda_x}^{\text{eff.}}(\vec{q}) \simeq \mu v_F |\vec{q}|. \quad (24)$$

where $\mu = \pm 1$ refers to the conduction (+1) and valence (−1) bands.

The resultant two-band model represented in Eq. (24) is written in the basis set $|1\rangle := (|c \uparrow\rangle, |a \uparrow\rangle)$, which is originated from the intervalley scattering between L_1 and L_2 points at the SnTe (001) surface. However, this form of Hamiltonian should respect the twofold rotation C_2 , which interchanges low-energy Dirac cones centered from Λ_x to Λ'_x . To calcify what is happening physically and to simplify the further analytical calculations, the unitary transformation associated with the inner physics (the role of both sublattices) of the system can be developed. Let us look for a unitary equivalence operator of the effective Hamiltonian $\hat{h}_{\Lambda_x}^{\text{eff.}}(\vec{q})$, which is defined as [48]

$$\hat{\mathbf{h}}'_{\Lambda_x}(\vec{q}) = \underline{\underline{U}} \hat{h}_{\Lambda_x}^{\text{eff.}}(\vec{q}) \underline{\underline{U}}^{-1}, \quad (25)$$

where

$$\underline{\underline{U}} = \frac{1}{2} \begin{pmatrix} \mathbf{i} + 1 & \mathbf{i} - 1 \\ \mathbf{i} + 1 & 1 - \mathbf{i} \end{pmatrix}, \quad (26)$$

is the unitary transformation, which changes the old basis set $|1\rangle$ and $|2\rangle$ to the new ones $|p_\pm\rangle$. Thereby, the effective Hamiltonian in the new basis set is written as

$$\hat{\mathbf{h}}'_{\Lambda_x}(\vec{q}) = v_F[\tilde{q}_x \hat{\tau}_y - \tilde{q}_y \hat{\tau}_x], \quad (27)$$

where the Pauli matrices $\hat{\tau} = (\hat{\tau}_0, \hat{\tau}_x, \hat{\tau}_y, \hat{\tau}_z)$ are defined on the new basis set mentioned above. It is necessary to mention that this rotated effective Hamiltonian has exactly the same eigenvalues as Eq. (24), implying that the physics of the Dirac

cones has not changed by this transformation. However, as it will be mentioned later, it helps a lot to find the corresponding electronic correlations between anions and cations simply. Obviously, the twofold rotation symmetry operator C_2 interchanges simply Hamiltonian for Dirac cone located at $+\Lambda_x$ to Λ'_x , thus [2,3]

$$C_2 \hat{\mathbf{h}}'_{\Lambda_x}(\vec{q}) C_2^{-1} = \hat{\mathbf{h}}'_{\Lambda'_x}(\vec{q}), \quad (28)$$

which is precisely that of Eq. (27). Indeed, the Hamiltonian around each of four Dirac cones have the same chirality, which is different from the case for graphene. So the same Hamiltonian on each Dirac cone is reasonable.

As for the physics of Λ_y and Λ'_y around X_2 point, we do not need to redo the calculations. The effective Hamiltonian on Dirac cones located around the valley X_2 can be derived by applying the fourfold symmetry operator C_4 on the effective Hamiltonian represented in Eq. (27), resulting in

$$C_4 \hat{\mathbf{h}}'_{\Lambda_x}(\vec{q}) C_4^{-1} = \hat{\mathbf{h}}'_{\Lambda_y}(\vec{K}) = v_F [\tilde{\mathcal{K}}_x \hat{\tau}_y - \tilde{\mathcal{K}}_y \hat{\tau}_x], \quad (29)$$

where $\tilde{\mathcal{K}}_x = \sqrt{\xi_2/\xi_1} \tilde{k}_x$ and $\tilde{\mathcal{K}}_y = \sqrt{\xi_1/\xi_2} \tilde{k}_y$.

Before going further, let us concisely list the Dirac Hamiltonians centered on $+\Lambda_x$, as the reference Dirac point for other Dirac points, as [49]

$$\hat{\mathbf{h}}'_{\Lambda_x}(\vec{q}) = \begin{pmatrix} 0 & f(\vec{q}) \\ f^*(\vec{q}) & 0 \end{pmatrix}, \quad (30)$$

where $f(\vec{q}) = -i v_F \tilde{q} \exp[-i \phi_{\vec{q}}]$ and $\phi_{\vec{q}} = \tan^{-1}(\tilde{q}_y/\tilde{q}_x)$. The phase factor $\exp[-i \phi_{\vec{q}}]$ changes for each Dirac cone, respecting the C_2 and C_4 rotation symmetries discussed above, such that one can extract four Dirac Hamiltonians by replacing its related phase factor on each Dirac point in the function $f(\vec{q})$.

To describe the pristine and doped Dirac cones as well as the interference between them, we divide the present section into two parts, pristine and doped TCI, in the following.

A. Effective low-energy of RKKY interaction in pristine TCI

Regarding very low-energy 2×2 Hamiltonian of Eq. (27) and its corresponding spectrum represented in Eq. (24), the \tilde{k} -space Green's function for the new set of eigenstates $|p_+\rangle$ and $|p_-\rangle$ around the valley X_1 is readily derived as

$$\begin{aligned} \underline{\underline{G}}^{\text{eff.}}(\bar{\Lambda}_x, \mathcal{E}) &= \frac{1}{\det} \begin{pmatrix} \tilde{\mathcal{E}} & i v_F \tilde{q} e^{-i \phi_{\vec{q}}} \\ -i v_F \tilde{q} e^{i \phi_{\vec{q}}} & \tilde{\mathcal{E}} \end{pmatrix} \\ &= \begin{pmatrix} G_{p_+ p_+}^{\text{eff.}, \Lambda_x}(\vec{q}, \mathcal{E}) & G_{p_+ p_-}^{\text{eff.}, \Lambda_x}(\vec{q}, \mathcal{E}) \\ G_{p_- p_+}^{\text{eff.}, \Lambda_x}(\vec{q}, \mathcal{E}) & G_{p_- p_-}^{\text{eff.}, \Lambda_x}(\vec{q}, \mathcal{E}) \end{pmatrix}, \end{aligned} \quad (31)$$

where $\det = \tilde{\mathcal{E}}^2 - v_F^2 \tilde{q}^2$. Correspondingly, the Green's function around the valley Λ'_x , Λ_y , and Λ'_y can be obtained using the C_2 and C_4 symmetries:

$$\underline{\underline{G}}^{\text{eff.}}(\bar{\Lambda}'_x, \mathcal{E}) = \underline{\underline{G}}^{\text{eff.}}(\bar{\Lambda}_x, \mathcal{E}), \quad (32a)$$

$$\underline{\underline{G}}^{\text{eff.}}(\bar{\Lambda}_y, \mathcal{E}) = \begin{pmatrix} G_{p_+ p_+}^{\text{eff.}, \Lambda_y}(\vec{q}, \mathcal{E}) & G_{p_+ p_-}^{\text{eff.}, \Lambda_y}(\vec{q}, \mathcal{E}) \\ G_{p_- p_+}^{\text{eff.}, \Lambda_y}(\vec{q}, \mathcal{E}) & G_{p_- p_-}^{\text{eff.}, \Lambda_y}(\vec{q}, \mathcal{E}) \end{pmatrix}, \quad (32b)$$

$$\underline{\underline{G}}^{\text{eff.}}(\bar{\Lambda}'_y, \mathcal{E}) = \underline{\underline{G}}^{\text{eff.}}(\bar{\Lambda}_y, \mathcal{E}), \quad (32c)$$

where

$$G_{p_{\pm} p_{\pm}}^{\text{eff.}, \Lambda_y}(\vec{K}, \mathcal{E}) = \frac{\tilde{\mathcal{E}}}{\tilde{\mathcal{E}}^2 - v_F^2 \tilde{K}^2}, \quad (33a)$$

$$G_{p_+ p_-}^{\text{eff.}, \Lambda_y}(\vec{K}, \mathcal{E}) = \frac{i v_F \tilde{K} e^{-i \phi_{\vec{K}}}}{\tilde{\mathcal{E}}^2 - v_F^2 \tilde{K}^2}, \quad (33b)$$

$$G_{p_- p_+}^{\text{eff.}, \Lambda_y}(\vec{K}, \mathcal{E}) = \frac{-i v_F \tilde{K} e^{i \phi_{\vec{K}}}}{\tilde{\mathcal{E}}^2 - v_F^2 \tilde{K}^2}. \quad (33c)$$

We note that features involving both sublattices with the same spins are indeed visible due to the sublattice mixing, discussing, in particular, the microscopic pseudospin taking place in the physics. Around the Dirac points, namely $|\vec{q}| \simeq |\vec{K}| \ll |\bar{\Lambda}_i|, |\bar{\Lambda}'_i|$ ($i \in \{x, y\}$) the new form of Eqs. (12) and (13) is given by, respectively,

$$\begin{aligned} G_{\gamma \zeta}^{\text{eff.}}(\mathcal{E}, \mathbf{R}, 0) &= 2 e^{i X_1 R_x} \cos(\Lambda_x R_x) G_{\gamma \zeta}^{\text{eff.}, \Lambda_x}(\mathcal{E}, \mathbf{R}, 0) \\ &\quad + 2 e^{i X_2 R_y} \cos(\Lambda_y R_y) G_{\gamma \zeta}^{\text{eff.}, \Lambda_y}(\mathcal{E}, \mathbf{R}, 0), \end{aligned} \quad (34)$$

and

$$G_{\gamma \zeta}^{\text{eff.}, \Lambda_i}(\mathcal{E}, \mathbf{R}, 0) = \frac{1}{\Omega_{\text{SBZ}}} \int_0^{\tilde{q}_c} \tilde{q} d\tilde{q} \int_0^{2\pi} d\phi_{\tilde{q}} e^{i \tilde{q} R \cos(\phi_{\tilde{q}} - \phi_R)} G_{\gamma \zeta}^{\text{eff.}, \Lambda_i}(\vec{q}, \mathcal{E}). \quad (35)$$

As an approximation, the same polar coordinate is used for Dirac cones to calculate the integrals shown in Eq. (35). Another remark refers to the limit of $\tilde{q}_c \rightarrow \infty$, which helps to solve the integrals easily.

1. Magnetic impurities on the same sublattices

We start with the same sublattices $\gamma = \zeta$. In this case, the involved terms in Eq. (31) are the same diagonal elements. The effective real-space Green's functions for the same sublattices with the same spin directions around $+\Lambda_x$ is calculated through

$$G_{\gamma \gamma}^{\text{eff.}, \Lambda_x}(\mathcal{E}, \mathbf{R}, 0) = \frac{\tilde{\mathcal{E}}}{\Omega_{\text{SBZ}}} \int_0^{\infty} \tilde{q} d\tilde{q} \int_0^{2\pi} d\phi_{\tilde{q}} e^{i \tilde{q} R \cos(\phi_{\tilde{q}} - \phi_R)} \frac{1}{\tilde{\mathcal{E}}^2 - v_F^2 \tilde{q}^2}. \quad (36)$$

Using the integrals

$$\begin{aligned} J_n(\tilde{q} R) &= \frac{i^{-n}}{2\pi} \int_0^{2\pi} d\phi_{\tilde{q}} e^{\pm i n \phi_{\tilde{q}}} e^{i \tilde{q} R \cos(\phi_{\tilde{q}} - \phi_R)}, \\ K_n(i \tilde{\mathcal{E}} R / v_F) &= -\frac{v_F^{n+2}}{\tilde{\mathcal{E}}^n} \int_0^{\infty} d\tilde{q} \frac{\tilde{q}^{n+1} J_n(\tilde{q} R)}{\tilde{\mathcal{E}}^2 - v_F^2 \tilde{q}^2}, \end{aligned} \quad (37)$$

in which the Bessel function J_n and the modified Bessel function of the second kind of integer orders n , K_n , are used. By this, we obtain

$$G_{\gamma \gamma}^{\text{eff.}, \Lambda_x}(\mathcal{E}, \mathbf{R}, 0) = -\frac{2\pi \tilde{\mathcal{E}}}{\Omega_{\text{SBZ}} v_F^2} K_0(i \tilde{\mathcal{E}} R / v_F). \quad (38)$$

Note that for the same sublattices made by the superposition of anions and cations $|p_+\rangle$ and $|p_-\rangle$, other electronic correlations $G_{\gamma \gamma}^{\text{eff.}, \Lambda'_x}(\mathcal{E}, \mathbf{R}, 0)$, $G_{\gamma \gamma}^{\text{eff.}, \Lambda_y}(\mathcal{E}, \mathbf{R}, 0)$, and $G_{\gamma \gamma}^{\text{eff.}, \Lambda'_y}(\mathcal{E}, \mathbf{R}, 0)$

are the same as Eq. (38), leading to

$$G_{\gamma\gamma}^{\text{eff}}(\mathcal{E}, \mathbf{R}, 0) = -\frac{4\pi\tilde{\mathcal{E}}}{\Omega_{\text{SBZ}}v_{\text{F}}^2} K_0(i\tilde{\mathcal{E}}R/v_{\text{F}}) [e^{iX_1R_x} \cos(\Lambda_x R_x) + e^{iX_2R_y} \cos(\Lambda_y R_y)]. \quad (39)$$

Now, we turn to the spin susceptibility tensor in Eq. (9). For the purposes of our present analysis, we briefly mention that in Eq. (10), the generic behavior of spins comes from the z component, and the formation of other spin directions will not be possible in the absence of an explicit spin flipping around the Dirac cones. In other words, the following equation is written based on the basis sets chosen along the z direction and it is independent of the spin direction, implying that for the other basis sets along the x and y direction, one finds the same results and, from this point, one would seek for the Heisenberg coupling as the effective exchange coupling. Thus, we have

$$C_{ij}^{\gamma\gamma}(\mathcal{E}, \mathbf{R}, 0) = \begin{cases} G_{\gamma\gamma}^{\text{eff}}(\mathcal{E}, \mathbf{R}, 0) G_{\gamma\gamma}^{\text{eff}}(\mathcal{E}, 0, \mathbf{R}) & \text{if } j = i = z \\ 0 & \text{if } j \neq i \end{cases}, \quad (40)$$

resulting in

$$\chi_{ii}^{\gamma\gamma}(\mathbf{R}, 0) = -\frac{1}{2\pi} \int_{-\infty}^{\mathcal{E}_{\text{F}}} d\mathcal{E} \text{Im} C_{ii}^{\gamma\gamma}(\mathcal{E}, \mathbf{R}, 0). \quad (41)$$

Since the Fermi level \mathcal{E}_{F} in SnTe (001) surface lies exactly in the zero energy (the doped case will be discussed in the next section), we use the property $\int_{-\infty}^0 = -\int_0^{\infty}$ as well as the relations ($z = \tilde{\mathcal{E}}R/v_{\text{F}}$)

$$K_n(iz) = -\frac{\pi}{2} e^{i\frac{n\pi}{2}} [Y_n(-z) - iJ_n(-z)], \quad (42a)$$

$$Y_n(-z) = (-1)^n [Y_n(z) + 2iJ_n(z)], \quad (42b)$$

$$J_n(-z) = (-1)^n J_n(z), \quad (42c)$$

where the specific function $Y_n(z)$ is the Neumann function [50]. Finally, we achieve the following expression:

$$\chi_{ii}^{\gamma\gamma}(\mathbf{R}, 0) = \frac{2\pi^3 \mathcal{F}(\mathbf{R})}{\Omega_{\text{SBZ}}^2 v_{\text{F}} R^3} \int_0^{\infty} dz z^2 Y_0(z) J_0(z), \quad (43)$$

and

$$\begin{aligned} \mathcal{F}(\mathbf{R}) &= \cos^2(\Lambda_x R_x) + \cos^2(\Lambda_y R_y) \\ &+ 2 \cos(\Lambda_x R_x) \cos(\Lambda_y R_y) \cos(X_1 R_x - X_2 R_y). \end{aligned} \quad (44)$$

Because of the oscillatory behavior of Bessel functions, the integral will not converge and one needs to multiply the integrand by a proper cutoff function $f(z, z_0) = \exp[-z/z_0]$ and then take the limit $z_0 \rightarrow \infty$ to achieve the convergence. The cutoff function comes in the integral to make sure large energies inside the integral are omitted. By this, we get $\lim_{z_0 \rightarrow \infty} \int_0^{\infty} dz f(z, z_0) z^2 Y_0(z) J_0(z) = 1/16$. Eventually, we have

$$\chi_{ii}^{\gamma\gamma}(\mathbf{R}, 0) = C \frac{\mathcal{F}(\mathbf{R})}{R^3}, \quad (45)$$

where $C = \pi^3/8 \Omega_{\text{SBZ}}^2 v_{\text{F}}$. The RKKY Hamiltonian is simply obtained as

$$\mathcal{H}_{\text{RKKY}}^{\gamma\gamma} = J_{\text{H}} \vec{s}_1 \cdot \vec{s}_2, \quad (46)$$

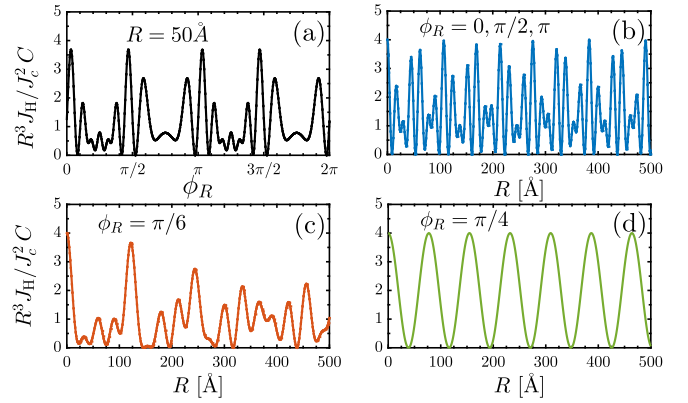


FIG. 5. Response of the RKKY interaction to the (a) angle and (b)–(d) distance between two magnetic impurities resided on the same sublattices in real space. In (a), the distance $R = 50 \text{ \AA}$ is fixed arbitrarily, while the angle is chosen as (b) $\phi_R = 0$, (c) $\phi_R = \pi/6$, and (d) $\phi_R = \pi/4$.

where $J_{\text{H}} = J_c^2 \chi_{ii}^{\gamma\gamma}(\mathbf{R}, 0)$ is the Heisenberg coupling between two spins in the same directions and with the same strengths. It should be pointed out that the RKKY Hamiltonian in 3D Weyl/Dirac semimetals and TI thin films contains additional Ising and the Dzyaloshinsky-Moriya terms, which lead to the different results [17,18]. Overall, the sign of the Heisenberg interaction parameter J_{H} reflects the fact that the impurities are aligned ferromagnetically at all and never transit to the antiferromagnetic phase, in contrast to the TI and TI thin films [13,41,51–56] for which the detailed structure of the Heisenberg spin interaction at long distances is switched to an antiferromagnetic state. This is a direct consequence of the interference between four Dirac cones, which does not allow the spin flipping. However, we may consider doping effects in the next sector where the magnetic phase transition covering a wide range of concentration is developed. We will come to this point later.

One observes that the RKKY interaction falls off with R^{-3} for long-range distances and oscillates as a combination of cosine functions with different Fermi wave vectors. Although the oscillatory structure factor $\mathcal{F}(\mathbf{R})$ is quite different than the Dirac materials (due to the interference between four anisotropic Dirac cones), the decay rate is that of the graphene one [14,15,57]. However, in 3D Weyl/Dirac semimetals, it has been theoretically shown that the RKKY interaction decomposing as the Heisenberg, the Dzyaloshinsky-Moriya, the spin-frustrated, and the Ising terms follows the decay rate of R^{-5} [17,18]. Moreover, the interference term in Weyl semimetals obeys a $\sin(2QR)$ stemming from $2Q$ separation of two nodal points in the first BZ. However, the oscillatory structure factor is quite different than our $\mathcal{F}(\mathbf{R})$.

To proceed, we work with the notations $R_x = R \cos(\phi_R)$ and $R_y = R \sin(\phi_R)$ for which we are free to choose the arbitrary direction of the indirect magnetic exchange-correlation. Regarding the behavior of $\mathcal{F}(\mathbf{R})$ [Eq. (44)], to explore the response of the RKKY interaction to the angle and distance between two magnetic impurities dwelled on the same sublattices, we plot Fig. 5. Several remarks are in order. The period in this RKKY response is π with respect to the angle ϕ_R [see

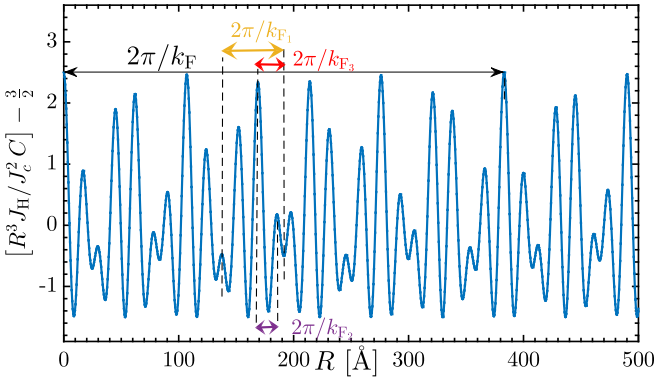


FIG. 6. The role of three Fermi wave vectors $k_{F1} = 2 \Lambda_x$, $k_{F2} = \Lambda_x + X_1$, and $k_{F3} = \Lambda_x - X_1$ on the RKKY interaction when the magnetic impurities are aligned to the same direction $\phi_R = 0$ and π or perpendicularly with $\phi_R = \pi/2$ on the same sublattices.

Fig. 5(a)], i.e., $\mathcal{F}(R, \phi_R) = \mathcal{F}(R, \pi + \phi_R)$. Here the distance between two magnetic impurities is set to 50 \AA for simplicity. The trend is not a fully sinusoidal function and different wave vectors (the frequency of the oscillations) are coming into play role in determining the period of oscillations. The primary source of such treatments in the system originates from the interference between four anisotropic Dirac cones, which have a relative $\pi/2$ phase difference. Otherwise, for the single Dirac cones, the results of the gapless phase of graphene or other semimetals are expected to come up [14,15,57].

In what follows, we particularly focus on three special possible cases, which lead to the same results. The same rates are expected to emerge for $\phi_R = 0, \pi/2$, and π due to the C_2 and C_4 rotation symmetries mentioned in Eqs. (28) and (29) (note that $\phi_R = 3\pi/2$ works as $\pi/2$). First, we assume that two magnetic impurities are located along the x direction ($\phi_R = 0$ and π), which allows us to set $R_y = 0$ and $R_x = \pm R$. In this case, two Dirac points Λ_x and Λ'_x only are involving in the above calculations. Second, in the same manner, assuming two magnetic impurities along the y direction ($\phi_R = \pi/2$), i.e., $R_x = 0$ and $R_y = R$ allows the contribution of two Dirac points Λ_y and Λ'_y only, i.e.,

$$\begin{aligned} \mathcal{F}(R) &= 1 + \cos^2(\Lambda_x R) + 2 \cos(\Lambda_x R) \cos(X_1 R) \\ &= \frac{3}{2} + \frac{1}{2} \cos(2 \Lambda_x R) + \cos([X_1 + \Lambda_x] R) \\ &\quad + \cos([X_1 - \Lambda_x] R). \end{aligned} \quad (47)$$

Note that the results are the same for the coordinates of Λ_y due to the valid C_4 rotation symmetry. Figure 5(b) shows the distance dependence of the $\mathcal{F}(\mathbf{R})$ for the phases $\phi_R = 0, \pi/2$, and π . We found that the period of the oscillations is around 383.1 \AA corresponding to the frequency of $2\pi/k_F = 0.0164 \text{ \AA}^{-1}$ (will be shown later in Fig. 6). The Fourier transformation may help in determining subfrequencies and harmonic components of the signal, however, the distance interval up to 500 \AA is sufficient to capture the frequency and period of the whole correlation function.

Also, it is possible to deduce the RKKY interaction response to the in-plane angle $\phi_R = \pi/4$. For this, the structure

factor reads

$$\mathcal{F}(R)|_{\phi_R=\pi/4} = [\cos(\sqrt{2}\Lambda_x R/2) + \cos(\sqrt{2}\Lambda_y R/2)]^2, \quad (48)$$

where the frequency of the cosine function gives rise to the Fermi wave vector $\sqrt{2}\Lambda_x/2$ (note that $\Lambda_x = \Lambda_y$), as shown in Fig. 5(d). However, for other phases such as $\phi_R = \pi/6$ or $\pi/3$, there is no periodic function. For this reason, we avoid the explicit expression of arbitrary phases in the present work. One, therefore, anticipates that the structure factor oscillates with distance, and from Fig. 5(c), it is clear that the amplitude of the oscillations decreases with a distance slightly (up to our regime, at least). This results from the in-plane angle effects, which showcase the weak magnetic screening effects in the long-range distances.

As a benchmark for the meaning of the subfrequencies mentioned in Fig. 5(b) and Eq. (47), here we adopted one further simplification with a view to consider the beating effects arising from the superposition of multiple momentum components, i.e., three Fermi wave vectors $k_{F1} = 2 \Lambda_x$, $k_{F2} = X_1 + \Lambda_x$, and $k_{F3} = X_1 - \Lambda_x$ (see Fig. 6). For a rock-salt structure of SnTe, i.e., face centered cubic lattice, $X_1 = X_2 = \pi/\sqrt{2}a \simeq 0.352 \text{ \AA}^{-1}$ ($a \simeq 6.3 \text{ \AA}$) and $\Lambda_x \simeq 0.057 \text{ \AA}^{-1}$ are used in the computations [58]. Note that the negative value of Heisenberg interaction is because of the deducted value of 1.5 and no antiferromagnetic state takes place in the system. Since Λ_x/X_1 is not very small, so the beating type is not clear. As conclusion there are at least three Fourier oscillation terms in the interference term, which contribute to the x or y direction.

2. Magnetic impurities on different sublattices

So far, we focused on the same sublattices. However, the electronic correlation between the wave functions of different sublattices may provide more information, since the phase factors come into play role in the interference effects of Dirac cones. Therefore, the effective real-space Green's functions for different sublattices around the Λ_x can be calculated via

$$\begin{aligned} G_{\gamma\zeta}^{\text{eff.},\Lambda_x}(\mathcal{E}, \mathbf{R}, 0) &= \frac{i v_F}{\Omega_{\text{SBZ}}} \int_0^\infty \tilde{q}^2 d\tilde{q} \int_0^{2\pi} d\phi_{\tilde{q}} \\ &\quad e^{-i\phi_{\tilde{q}}} \frac{e^{i\tilde{q}R \cos(\phi_{\tilde{q}} - \phi_R)}}{\tilde{\mathcal{E}}^2 - v_F^2 \tilde{q}^2}. \end{aligned} \quad (49)$$

With the help of Eqs. (37) and (42), we get

$$G_{\gamma\zeta}^{\text{eff.},\Lambda_x}(\mathcal{E}, \mathbf{R}, 0) = \frac{2\pi \tilde{\mathcal{E}}}{\Omega_{\text{SBZ}} v_F^2} e^{-i\phi_R} K_1(i \tilde{\mathcal{E}} R / v_F), \quad (50)$$

and $G_{\gamma\zeta}^{\text{eff.},\Lambda'_x}(\mathcal{E}, \mathbf{R}, 0) = G_{\gamma\zeta}^{\text{eff.},\Lambda_y}(\mathcal{E}, \mathbf{R}, 0) = G_{\gamma\zeta}^{\text{eff.},\Lambda'_y}(\mathcal{E}, \mathbf{R}, 0) = G_{\gamma\zeta}^{\text{eff.},\Lambda_x}(\mathcal{E}, \mathbf{R}, 0)$, leading to [see Eq. (34)]

$$\begin{aligned} G_{\gamma\zeta}^{\text{eff.}}(\mathcal{E}, \mathbf{R}, 0) &= \frac{4\pi \tilde{\mathcal{E}}}{\Omega_{\text{SBZ}} v_F^2} e^{-i\phi_R} K_1(i \tilde{\mathcal{E}} R / v_F) \\ &\quad \times [e^{iX_1 R_x} \cos(\Lambda_x R_x) + e^{iX_2 R_y} \cos(\Lambda_y R_y)]. \end{aligned} \quad (51)$$

To calculate the spin susceptibility tensor, we use

$$C_{ij}^{\gamma\zeta}(\mathcal{E}, \mathbf{R}, 0) = \begin{cases} G_{\gamma\zeta}^{\text{eff}}(\mathcal{E}, \mathbf{R}, 0) G_{\gamma\zeta}^{\text{eff}}(\mathcal{E}, 0, \mathbf{R}) & \text{if } j = i = z \\ 0 & \text{if } j \neq i \end{cases}, \quad (52)$$

which leads to

$$\chi_{ii}^{\gamma\zeta}(\mathbf{R}, 0) = + \frac{2\pi^3 \mathcal{G}(\mathbf{R})}{\Omega_{\text{SBZ}}^2 v_F R^3} \int_0^\infty dz z^2 Y_1(z) J_1(z), \quad (53)$$

where

$$\begin{aligned} \mathcal{G}(\mathbf{R}) = & \cos^2(\Lambda_x R_x) + \cos^2(\Lambda_y R_y) \\ & + [2 \cos(\Lambda_x R_x) \cos(\Lambda_y R_y) \cos(X_1 R_x - X_2 R_y)]. \end{aligned} \quad (54)$$

Again, using the cutoff function $f(z, z_0) = \exp[-z/z_0]$, we have $\lim_{z_0 \rightarrow \infty} \int_0^\infty dz z f(z, z_0) z^2 Y_1(z) J_1(z) = -3/16$ and

$$\chi_{ii}^{\gamma\zeta}(\mathbf{R}, 0) = -D \frac{\mathcal{G}(\mathbf{R})}{R^3}, \quad (55)$$

where $D = 3\pi^3/8 \Omega_{\text{SBZ}}^2 v_F$. In this case, arbitrary directions for residing the magnetic impurities can be chosen due to the angle ϕ_R . Similarly, one can argue that the same RKKY Heisenberg Hamiltonian as Eq. (46) is obtained because on the spin scale of the interacting terms change in the energy cancel out.

Interestingly, a similar phase function is seen. This stems from the square Bravais lattice of the SnTe(001) surface and the symmetry between the \vec{k} points of the SBZ on the same and different sublattices, in contrast to the anisotropic responses in graphene [14,15,57]. Thus, the previous arguments can be repeated to justify the oscillatory behavior of the response of the RKKY interaction to the distance between two magnetic impurities resided on different sublattices.

To finish this part, an additional interpretation/comparison is needed. For enough of interest, one notices that the phase of SnTe (001) surface in the pristine state is ferromagnetic (FM) and antiferromagnetic (AFM), respectively, when the magnetic impurities reside on the same sublattices and different ones.

B. Effective low-energy of RKKY interaction in doped TCI

Here we deduce the susceptibility provided in Eq. (41) for the resided magnetic impurities on the same sublattices in the case of nonzero \mathcal{E}_F , i.e., when the system is doped. Two scenarios are needed to be discussed here, (i) electron-doped and (ii) hole-doped corresponding to $\mathcal{E}_F > 0$ and $\mathcal{E}_F < 0$, respectively.

1. Magnetic impurities on the same sublattices

We straightforwardly start with Eq. (41) so that the integral from $-\infty$ to \mathcal{E}_F is expanded as $\int_{-\infty}^{\mathcal{E}_F} = -\int_0^\infty + \int_0^{\mathcal{E}_F}$. So, it is expected to have an extra \mathcal{E}_F -dependent term in Eq. (43) in the presence of doping. Let us write down [15,57,59,60]

$$\tilde{\chi}_{ii}^{\gamma\gamma}(\mathbf{R}, 0) = \chi_{ii}^{\gamma\gamma}(\mathbf{R}, 0) - \frac{2\pi^3 \mathcal{F}(\mathbf{R})}{\Omega_{\text{SBZ}}^2 v_F R^3} \int_0^{x_F} dz z^2 Y_0(z) J_0(z), \quad (56)$$

where $\tilde{\chi}_{ii}^{\gamma\gamma}(\mathbf{R}, 0)$ is the doped susceptibility and $\chi_{ii}^{\gamma\gamma}(\mathbf{R}, 0)$ is the undoped susceptibility. Easily, one finds

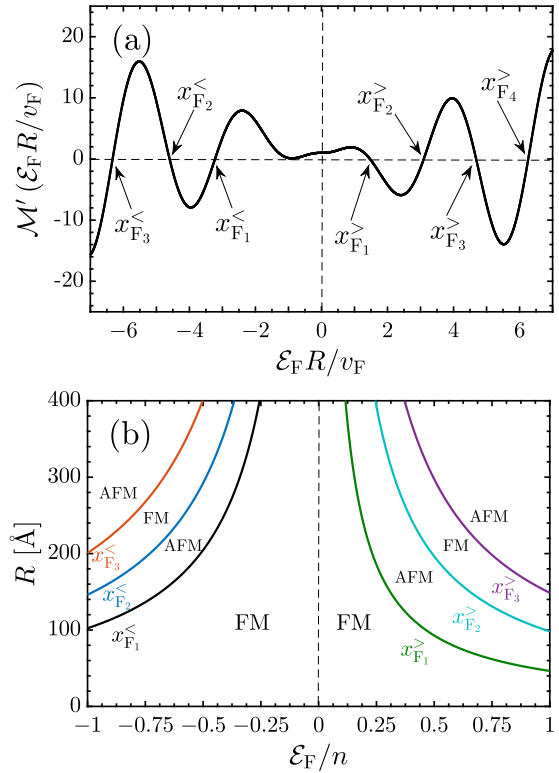


FIG. 7. (a) The asymmetric function $\mathcal{M}'(x_F)$ in Eq. (57) versus $x_F = \mathcal{E}_F R / v_F$. Different critical distance- and Fermi energy-dependent points are labeled at which the FM-to-AFM (positive to negative sign changing) and vice versa takes place. $\mathcal{E}_{F_i}^<$ ($\mathcal{E}_{F_i}^>$) refers to the electron (hole) doping. (b) shows the magnetic phase diagram of the distance between two magnetic impurities on the same sublattices as a function of the Fermi energy for four different phase transition parameters.

$\int_0^{x_F} dz z^2 Y_0(z) J_0(z) = -\frac{x_F}{2\sqrt{\pi}} G_{2,4}^{2,1} \left(1, 1, -\frac{1}{2}, 1 \mid x_F^2 \right)$, where G is the Meijer function [61,62] and $x_F = \frac{\mathcal{E}_F R}{v_F}$. Thereby, we gain

$$\tilde{\chi}_{ii}^{\gamma\gamma}(\mathbf{R}, 0) = \chi_{ii}^{\gamma\gamma}(\mathbf{R}, 0) \underbrace{\left[1 + \frac{8x_F}{\sqrt{\pi}} G_{2,4}^{2,1} \left(1, 1, -\frac{1}{2}, 1 \mid x_F^2 \right) \right]}_{\mathcal{M}'(x_F)}. \quad (57)$$

In this case, the sign of \tilde{J}_H in the heart of $\tilde{\chi}_{ii}^{\gamma\gamma}(\mathbf{R}, 0)$ changes, called a magnetic phase transition, due to the intrinsic oscillatory behavior of $\mathcal{M}'(x_F)$. The physical origin of this transition can be understood from the fact that charge current flow and spin current flow in TCIs is coupled already and the new charge current induced by the electrons and/or holes leads to the spin flipping depending on the charge concentration.

In Fig. 7, we numerically derive that the first FM-to-AFM phase transition for electron-doping $\mathcal{E}_{F_i}^>$ emerges at critical $x_{F_1}^> = 1.46$. The second point appears at $x_{F_2}^> = 3.09$ and accordingly, one obtains $x_{F_3}^> = 4.68$, $x_{F_4}^> = 6.26$ and so on. Interestingly, one simply finds $x_{F_{i+1}}^> - x_{F_i}^> \simeq 1.6$ as the distance between a FM-to-AFM and AFM-to-FM transition in the presence of electron doping. However, this does not appear as soon as the holes are doped to the SnTe (001) surface. This can be tracked from $\mathcal{M}'(x_F)$ shown in Fig. 7(a) in which the

FM-to-AFM and AFM-to-FM transitions take place at $|x_{F_1}^<| = 3.22$, $|x_{F_2}^<| = 4.60$, $|x_{F_3}^<| = 6.32$ and so on, which clearly are different than the electron-doped TCI. This case makes the fact that the required distance between magnetic impurities obeys the above-estimated relation $|x_{F_{i+1}}^<| - |x_{F_i}^<| \simeq 1.6$. Obviously, the presence of the Fermi level leads to different results compared to that of undoped case. It should be mentioned that \mathcal{E}_F in the above equation cannot be larger than n and we prefer to increase it up to the critical intervalley scattering energy n for which our low-energy theory is valid.

Regarding the asymmetric form of $\mathcal{M}'(x_F)$ concerning the distance R and the Fermi level \mathcal{E}_F (the criterion distance would be inversely proportional to the Fermi level), the phase diagram of the doped system, Fig. 7(b), is also not symmetric regarding the type of doping, $\mathcal{E}_F^>$ or $\mathcal{E}_F^<$. As it was mentioned before, the criterion distance between two magnetic impurities, is inversely proportional to \mathcal{E}_F , as expected from the phase transition parameter $x_F = \mathcal{E}_F R / v_F$; beneath the curve for first points $x_{F_1}^>$ and $x_{F_1}^<$ is taken as the base phase of the system (FM), while above the curves are characteristic of AFM phase, reflecting the fact that the doped TCI is essentially the set of FM and AFM phases depending on the R and Fermi level.

Now that we have discussed the general treatments of the phase diagram for doped TCI, for the sake of completeness on the low and high limit of $\mathcal{M}'(x_F)$, we look at asymptotic behavior of $R^3 \tilde{J}_H / J_c^2 C = \mathcal{F}(\mathbf{R}) \mathcal{M}'(x_F)$ taken from Eq. (57),

$$\lim_{x_F \rightarrow \infty} \frac{R^3 \tilde{J}_H}{J_c^2 C} \simeq \mathcal{F}(\mathbf{R}) [2 \cos(2x_F) + 8x_F \sin(2x_F)], \quad (58)$$

where at large-enough $x_F \gg 1$, it is shortened to $R^3 \tilde{J}_H / J_c^2 C \simeq x_F \mathcal{F}(\mathbf{R}) \sin(2x_F)$. As a result of this, at large distances, \tilde{J}_H is expected to decay as R^{-2} (because $x_F = \mathcal{E}_F R / v_F$), which behaves the same as conventional 2D systems [15,57,59,60]. Furthermore, in this regime, RKKY interaction increases with Fermi energy. Moreover, it obviously shows that the electron-hole symmetry is preserved at long distances or highly doped states. On the other hand, for $x_F \ll 1$, it also simply reads as the following:

$$\lim_{x_F \rightarrow 0} \frac{R^3 \tilde{J}_H}{J_c^2 C} \simeq \mathcal{F}(\mathbf{R}) \left[1 + \frac{32x_F^3}{9\pi} (1 - 3t - 3 \log(x_F/2)) \right], \quad (59)$$

where $t \simeq 0.577$ [61,62]. It is clear from the above equation that at short distances, RKKY exchange coupling decays as R^{-3} , and there is no electron-hole symmetry in this regime, which corresponds to short distances or Fermi energies close to the zero modes. This is the reason for the lack of symmetry in the phase diagram of Fig. 7(b) at weak doping.

The fact that charge fluctuation becomes strong with the increase of electron doping is consistent with the enhancement of the RKKY response at zero temperature with increasing \mathcal{E}_F/n . This can be understood from the linear dependence of DOS to the energy (see Fig. 3). Looking at Eq. (6), one notices that an increase in the electron doping corresponds to a larger DOS. On the other hand, from Eq. (41), the RKKY exchange coupling treats with the local DOS as the following:

$$\chi_{ii=zz}^{\gamma\gamma}(\mathbf{R}, 0) \propto \mathcal{D}^0(\mathcal{E}_F) \text{Re}[G_{\gamma\gamma}^0(\mathcal{E}_F, \mathbf{R}, 0)], \quad (60)$$

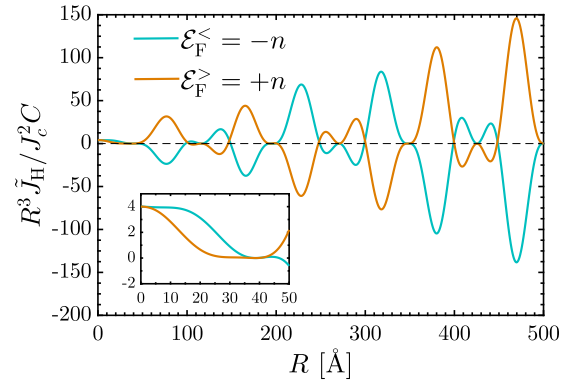


FIG. 8. The response of the RKKY interaction in the presence of both electron and hole doping to the distance R between two magnetic impurities on the same sublattices.

where $\mathcal{D}^0(\mathcal{E}_F) \propto \mathcal{E}_F$ is the DOS at the Fermi level, which linearly depends on the energy (see Fig. 3) in Dirac materials. Hence, $\chi_{ii=zz}^{\gamma\gamma}(\mathbf{R}, 0)$ increases linearly with \mathcal{E}_F . So we expect to have a stronger RKKY response when increasing the electron or hole concentration. In other words, electron doping may increase the scattering rate of charge carriers and affect indirectly the exchange RKKY interaction, which is concentration dependent.

It should be mentioned that as represented in Eq. (57), $\mathcal{M}'(x_F)$ is independent of ϕ_R , so the doped susceptibility behaves with the direction of the undoped susceptibility. Indeed, ϕ_R dependence of RKKY interaction is originated from the interference term, which is periodic on the direction of magnetic impurities, $\mathcal{F}(R, \phi_R) = \mathcal{F}(R, \pi + \phi_R)$. Despite the ϕ_R dependence of RKKY interaction, it is obvious that there is no period in R for the doped TCI as well. The reason is related to the Meijer function, which is not periodic in terms of R .

For the undoped TCI, the RKKY coupling was shown to be monotonically FM in terms of R (see Fig. 5), while for the doped TCI, it has an oscillatory behavior giving rise to subsequent FM-to-AFM transitions and vice versa, as represented in Fig. 8. For both electron- and hole-doped TCI, one may expect the symmetric response to the distance. However, as mentioned before, for long-range distances the Heisenberg term decays as R^{-2} , while the decay function is proportional to R^{-3} for short distances. This, in turn, leads to the symmetric responses to large-enough R , while to the asymmetric one for the small-enough R .

Another remark can be explored for $R^3 \tilde{J}_H / J_c^2 C$ as a function of \mathcal{E}_F/n , to understand the distance and Fermi energy-dependent electron-hole symmetry concept. In this regard, we use the following procedures: (i) We assume that R is material independent and is fixed at 50 Å and 500 Å with $\phi_R = \pi/4$ (there is no physical reason for this phase and other angles can be chosen as well; single-frequency oscillatory behavior of this phase is the main reason for this selection), short and long range. (ii) We examine the electron and hole doping (\mathcal{E}_F/n), which varies from -1 to $+1$. We find in Fig. 9 that our results nicely produce the global feature of our purpose. In particular, the calculated data show a nice agreement with the expectation explained in Eqs. (58) and (59). For short-range

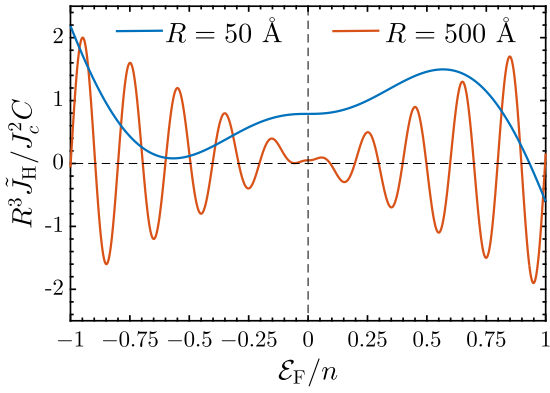


FIG. 9. $R^3 J_H / J_c^2 C$ as a function of the Fermi energy \mathcal{E}_F / n for short-range distance $R = 50 \text{ \AA}$ and long-range distance $R = 500 \text{ \AA}$ between two magnetic impurities on the same sublattices at $\phi_R = \pi/4$.

$R = 50 \text{ \AA}$, there is no electron-hole symmetry even for strong doping, while it can be reported for long-range $R = 500 \text{ \AA}$ and strong doping. Interestingly, this reconfirms our claim that one should not expect such symmetry at a long-range distance and weak doping, as can be seen around $\mathcal{E}_F / n = 0$ in the red curve. Although the global agreement with the expectations is satisfactory, some deviations from the experimental data may happen since our theory is approximated to the low-energy region. Note that the period of oscillations in Fig. 9 for the long-distance $R = 500 \text{ \AA}$ is $2 x_F$ [see Eq. (58)].

2. Magnetic impurities on different sublattices

To discuss the RKKY response in the case that two magnetic impurities are sitting on different sublattices, we rewrite Eq. (55) in terms of the Fermi energy \mathcal{E}_F in a similar way to Eq. (56) as

$$\tilde{\chi}_{ii}^{\gamma\zeta}(\mathbf{R}, 0) = \chi_{ii}^{\gamma\zeta}(\mathbf{R}, 0) + \frac{2\pi^3 \mathcal{G}(\mathbf{R})}{\Omega_{\text{SBZ}}^2 v_F R^3} \int_0^{x_F} dz z^2 Y_1(z) J_1(z), \quad (61)$$

where $\tilde{\chi}_{ii}^{\gamma\zeta}(\mathbf{R}, 0)$ is the doped susceptibility and $\chi_{ii}^{\gamma\zeta}(\mathbf{R}, 0)$ is the undoped susceptibility. Within the same manner, one calculates $\int_0^{x_F} dz z^2 Y_1(z) J_1(z) = -\frac{x_F}{2\sqrt{\pi}} G_{2,4}^{2,1} \left(1, 2, -\frac{1}{2}, \frac{3}{2}, 0 \middle| x_F^2 \right)$, where again $x_F = \frac{\mathcal{E}_F R}{v_F}$. Thus, we have

$$\tilde{\chi}_{ii}^{\gamma\zeta}(\mathbf{R}, 0) = \chi_{ii}^{\gamma\zeta}(\mathbf{R}, 0) \underbrace{\left[1 - \frac{8x_F}{3\sqrt{\pi}} G_{2,4}^{2,1} \left(1, 2, -\frac{1}{2}, \frac{3}{2}, 0 \middle| x_F^2 \right) \right]}_{\mathcal{M}''(x_F)}. \quad (62)$$

The physical origin of spin flipping in this case is the same as before. Thus, let us consider the mathematical origin of sign changing in $\tilde{\chi}_{ii}^{\gamma\zeta}(\mathbf{R}, 0)$. $\mathcal{M}''(x_F)$ is interpreted as the set of the oscillations with an asymmetrical trend making different numbers of roots in the case of electron and hole doping that is included in x_F quantity. Here, in Fig. 10(a), we find $x_{F_1}^> = 1.17$, $x_{F_2}^> = 2.94$, $x_{F_3}^> = 4.58$, and $x_{F_4}^> = 6.18$ for the electron carrier side, while $|x_{F_1}^<| = 3.32$, $|x_{F_2}^<| = 4.29$, and $|x_{F_3}^<| = 6.37$ for the hole carrier side. Again, we conclude that the regular

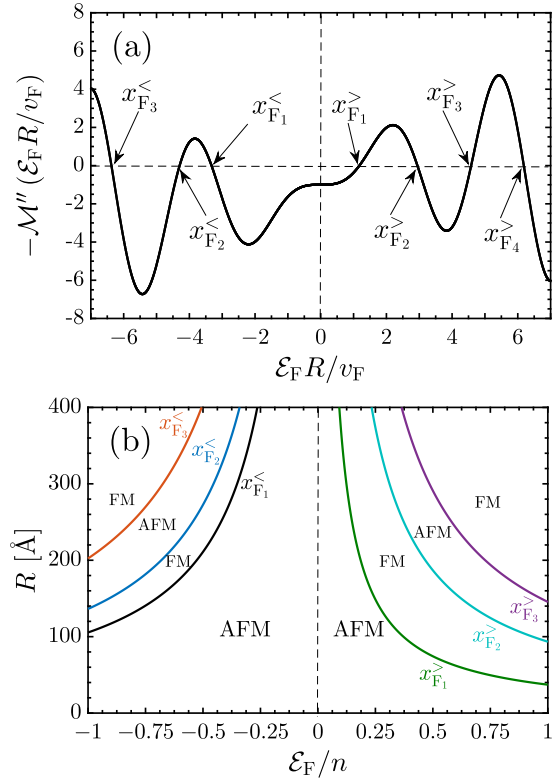


FIG. 10. (a) The asymmetric function $\mathcal{M}''(x_F)$ in Eq. (62) versus $x_F = \mathcal{E}_F R / v_F$. $\mathcal{E}_{F_i}^<$ ($\mathcal{E}_{F_i}^>$) refers to the electron (hole) doping. The magnetic phase diagram of distance between two magnetic impurities on different sublattices as a function of the Fermi energy is printed in (b) for four different phase transition parameters.

sign changing of \tilde{J}_H obeys the relation $|x_{F_{i+1}}| - |x_{F_i}| \simeq 1.6$ for both electron- and hole-doping cases.

A schematic representation of phases adopted by the points corresponding to the phase transitions is plotted in Fig. 10(b) over a range of varying parameters distance R and the Fermi energy \mathcal{E}_F . When two magnetic impurities reside on different sublattices, the description of FM and AFM phases is not the same as that of the same sublattices. This implies that the wide area corresponding to the base phase of the SnTe (001) surface refers to the AFM phase, while this happened for the FM phase in the case of the same sublattices.

In the rest of this section, we calculate the asymptotic behavior of $-R^3 \tilde{J}_H / J_c^2 D = \mathcal{G}(\mathbf{R}) \mathcal{M}''(x_F)$ to understand the limits of low and high x_F , which is useful for treating the dependence of the Heisenberg coupling to the distance and Fermi energy. Thereby, we would write [15,57,59,60]

$$\lim_{x_F \rightarrow \infty} -\frac{R^3 \tilde{J}_H}{J_c^2 D} \simeq \mathcal{G}(\mathbf{R})_{x_F} \sin(2x_F), \quad (63a)$$

$$\lim_{x_F \rightarrow 0} -\frac{R^3 \tilde{J}_H}{J_c^2 D} \simeq \mathcal{G}(\mathbf{R}) \left[1 - \frac{16x_F^3}{9\pi} \right]. \quad (63b)$$

So, for small-enough x_F , the RKKY response is asymmetric if $x_F \mapsto -x_F$ [see Eq. (63b)], while it is symmetric for large-enough x_F [see Eq. (63a)]. Moreover, at short distances, RKKY exchange coupling decays as R^{-3} , while it decays as R^{-2} at long distance. By these, we mean that the decay rate is

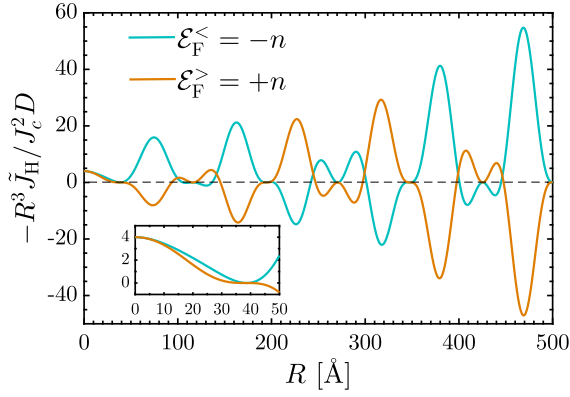


FIG. 11. The response of the RKKY interaction in the presence of both electron and hole doping to the distance R between two magnetic impurities on different sublattices.

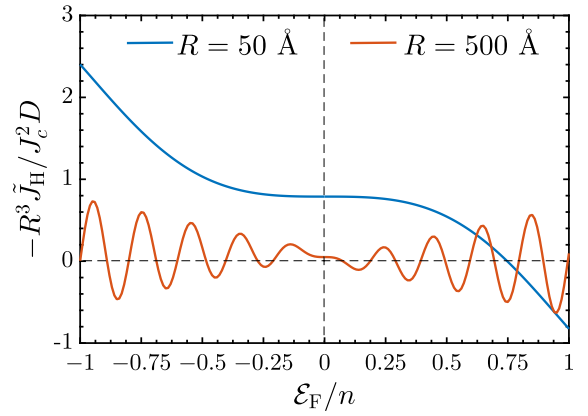


FIG. 12. $-R^3 J_H / J_c^2 D$ as a function of the Fermi energy \mathcal{E}_F / n for short-range distance $R = 50 \text{ \AA}$ and long-range distance $R = 500 \text{ \AA}$ between two magnetic impurities on different sublattices at $\phi_R = \pi/4$.

the same whether the impurities are on the same or different sublattices. Although these cannot be seen in Fig. 10, we will address these points in the following by focusing on the details of distance and Fermi energy parameters. In general, we have three varying parameters, namely ϕ_R , R , and \mathcal{E}_F .

In this paragraph, we intend to show that $-R^3 \tilde{J}_H / J_c^2 D$ as a function of angle ϕ_R for two different Fermi energies $\mathcal{E}_F^< = -n$ and $\mathcal{E}_F^> = +n$ and the same distance $R = v_F / n$, i.e., $x_F^< = -1$ and $x_F^> = +1$ possesses the same trend because the coefficient $\mathcal{G}(\mathbf{R})$ behaves independent of the Fermi energy. However, one expects different amplitudes for $\mathcal{G}(\mathbf{R})$ in the presence of doping because of the extra \mathcal{E}_F -dependent $\mathcal{M}''(x_F)$ and corresponding terms at low and high x_F .

Figure 11 corresponds to $-R^3 \tilde{J}_H / J_c^2 D$ as a function of R for $\mathcal{E}_F^< = -n$ and $\mathcal{E}_F^> = +n$ at varying $x_F = \mathcal{E}_F R / v_F$ with $\phi_R = \pi/4$. We observe that there is no certain distance difference, in contrast to the previous case, in which the sign changing happens for \tilde{J}_H when the impurities reside on different sublattices. This is independent of the Fermi energy. However, our analysis in Eq. (63) can be met here for $R \rightarrow 0$ and $R \rightarrow \infty$, i.e., when the system is subjected to the electron and hole doping through the same Fermi energy strength but opposite signs, the response is not the same for the FM and AFM phases at short distances, while when R moves forward, they get close to each other and one expects to have the same strengths at large-enough R .

In order to find the explicit description of magnetic phase transition in terms of the Fermi energy, we plot $-R^3 \tilde{J}_H / J_c^2 D$ as a function of \mathcal{E}_F / n (both positive and negative signs) in Fig. 12 at two short $R = 50 \text{ \AA}$ and long $R = 500 \text{ \AA}$ distances. Following the previous analysis and Eqs. (63a) and (63b), in the limit of $x_F \rightarrow 0$, one understands that $\mathcal{E}_F R \rightarrow 0$ and this, in turn, means that for short distances $R = 50 \text{ \AA}$, the electron-hole symmetry is not valid anymore independent of \mathcal{E}_F , however, in the limit of $x_F \rightarrow \infty$, one finds that $\mathcal{E}_F R \rightarrow \infty$, implying that at long distances $R = 500 \text{ \AA}$ the doping should be strong enough to meet the electron-hole symmetry. As can be seen in Eq. (63b), the period of oscillations in Fig. 12 for the long-distance $R = 500 \text{ \AA}$ is $2x_F$.

VI. DISCUSSION

The susceptibilities studied in Sec. IV are intrinsic to the gapless phase of the Dirac cones in the absence or presence of electron and/or hole doping. As stated before, the gapped phase of Dirac cones may be considered as well in the presence of other possible perturbations such as perpendicular magnetic field and ferroelectric distortion [3]. The breakdown of the lattice symmetry is governed by such external factors. It is necessary to mention that surface roughness, which is inevitable in experiment requires more attention. Roughness, which is essentially time-reversal invariant, breaks the mirror symmetry in random places locally. But in the macroscopic view and on the average, if roughness causes slowly variation in the atomic positions, one may still observe sharp peaks in the x-ray diffraction from the Bragg planes. So in this case, macroscopically, the mirror symmetry is preserved while it fails inside the domain walls [2]. In such situations, our results of gapless surface states, at long-range distances is still valid while for short-range distances, RKKY response obeys from the gapped Hamiltonian. On the other hand, in the sense of x-ray diffraction peaks, roughness may cause a damage in the crystallinity of the material. So the mirror symmetry would be no longer preserved. In this case, a gap is opened in the band spectrum and RKKY interaction is calculated by a specific formulation, which is out of the scope of the present paper. The new formulation including the perturbations manifestly acts to induce the gap as well as the exchange field of magnetic impurities themselves and thus leads to a significantly more involved set of responses. Nevertheless, the anisotropic interactions such as Dzyaloshinskii-Moriya coupling and/or the origin of anisotropic interactions such as Rashba spin-orbit coupling may modulate the model as well. We postpone a detailed analysis of the perturbed susceptibility including all these effects to a followup study.

It should be pointed out that the electron and hole doping are taken to be material dependent, however, we stress that the investigations in the present paper are allowed for SnTe and related alloys only, not for all TCIs. Moreover, we examined the RKKY response at zero temperature in our model and the finite-temperature version of the results will be left to come

in our future research utilizing the temperature-dependent \mathcal{E}_F under the grand-canonical ensemble. Additionally, as we mentioned during the elaboration of the low-energy effective Hamiltonian, four Dirac cones approximation is valid for energies lower than the quantity n . So the doped level should be lower than this quantity and at low-level doping, smaller than n , the bulk of TCI would remain a gapped insulator and our results on RKKY interaction are still valid. Regarding the control of the electron or hole doping only on the surface of TCI, we should mention that it is long well known that doped ions enter substitutionally instead of Sn/Pb atoms in (Sn/Pb)Te materials [10,42,63–65]. In our model, the bulk atoms are substitutionally doped by doped ions with a chemical potential adjusted inside the bulk gap. So there are no free carriers inside the bulk while they are present on the surface. It is deduced that by the low-level bulk doping especially in the vicinity of the surface, the chemical potential varies ranging from $-n$ to $+n$, the validation range of the effective Hamiltonian. As a result, we do not need to have doped ions exactly located on the surface of TCI.

As the last comment, we would briefly think of the case that the magnetic impurities are laid down on the bond centers of the sublattices. In this case, the RKKY response is the sum of the site responses and the spin susceptibility is written as $\chi_{zz}^{\text{bond}}(\mathbf{R}, 0) = 2\chi_{zz}^{\gamma\gamma}(\mathbf{R}, 0) + \chi_{zz}^{\gamma\zeta}(\mathbf{R}, 0) + \chi_{zz}^{\zeta\gamma}(-\mathbf{R}, 0)$. Accordingly, the interference of such a situation can be obtained by plugging in the individual $\mathcal{F}(\mathbf{R})$ and $\mathcal{G}(\mathbf{R})$ ones. As a direct consequence of this, we would conclude that the resulting interference only differs compared to that of graphene, and, for this reason, we avoid repeating this unnecessary calculation.

VII. SUMMARY

Understanding the interaction between magnetic impurities on the surface of TCIs is essential for many spintronic purposes. This is interesting because of the presence of multiple surface states in TCIs, which are topologically protected by the mirror symmetry.

In this paper, we have considered the case of (001) surface of SnTe as a TCI subjected to magnetic impurities. We derive through an effective low-energy two-band model the RKKY coupling between two magnetic impurities resided on the same and different sublattices in the absence and presence of electron and hole doping. The potential of our two-band

model is examined by the electronic band structure, resulting in a valuable prediction of the full implementation of RKKY coupling (i.e., followed by the four-band model). Within such a proper low-energy approximation, all possible RKKY responses, spin susceptibilities, have calculated analytically. These results capture the data for different parameters, namely the angle and distance between two magnetic impurities, and the Fermi level.

The key analytic argument illustrates that the RKKY coupling on the SnTe (001) surface with four Dirac cones behaves as graphene independent of the doping effect or the position of impurities. However, the main difference can be tracked from the interference term in which multiple wave vectors play the role to determine the RKKY responses, while a single wave vector is adequate in graphene. On the other hand, the base phase of the system for magnetic impurities on the same and different sublattices is FM and AFM, respectively. The decay rate of spin susceptibility with the distance between impurities is that of R^{-3} in the undoped TCIs, while it is, respectively, R^{-3} and R^{-2} in the doped case for short-range and long-range interaction.

Key physics of our results has revealed in the phase diagram of magnetic states covered in the presence of both electron and hole doping. The systematic dependence of distance on the Fermi level has inherited the FM and AFM phases so that host electrons at the same or different sublattices give a specific magnetic order depending on the distance and doping concentration. This, in turn, originates from the contribution of different wave vectors to the interference between surface Dirac cones. Generically, in the presence of doping, the FM-to-AFM phase transition and vice versa occur so that the sign of Heisenberg coupling switches.

To what extent the magnetic impurities are necessary ingredients for spintronic devices in logic applications, our results would be the subject of a lively discussion. The intriguing next step would be dealing with the exchange field induced by the magnetic impurities to break the mirror symmetry and to open a gap in the SnTe (001) surface to tailor both the topological and magnetic phases.

ACKNOWLEDGMENT

H.C. acknowledges the Institute for Research in Fundamental Sciences (IPM) for hospitality and support in capacity of Resident Researcher Program.

-
- [1] M. Z. Hasan and C. L. Kane, Colloquium: Topological insulators, *Rev. Mod. Phys.* **82**, 3045 (2010).
 - [2] T. H. Hsieh, H. Lin, J. Liu, W. Duan, A. Bansil, and L. Fu, Topological crystalline insulators in the snite material class, *Nature Commun.* **3**, 982 (2012).
 - [3] M. Serbyn and L. Fu, Symmetry breaking and Landau quantization in topological crystalline insulators, *Phys. Rev. B* **90**, 035402 (2014).
 - [4] Y. Tanaka, Z. Ren, T. Sato, K. Nakayama, S. Souma, T. Takahashi, K. Segawa, and Y. Ando, Experimental realization of a topological crystalline insulator in snite, *Nature Phys.* **8**, 800 (2012).
 - [5] C. Yan, J. Liu, Y. Zang, J. Wang, Z. Wang, P. Wang, Z.-D. Zhang, L. Wang, X. Ma, S. Ji, K. He, L. Fu, W. Duan, Q.-K. Xue, and X. Chen, Experimental Observation of Dirac-Like Surface States and Topological Phase Transition in $\text{pb}_{1-x}\text{sn}_x\text{Te}(111)$ Films, *Phys. Rev. Lett.* **112**, 186801 (2014).
 - [6] Y. Tanaka, T. Shoman, K. Nakayama, S. Souma, T. Sato, T. Takahashi, M. Novak, K. Segawa, and Y. Ando, Two types of Dirac-cone surface states on the (111) surface of the topological crystalline insulator snite, *Phys. Rev. B* **88**, 235126 (2013).
 - [7] S. Safaei, P. Kacman, and R. Buczko, Topological crystalline insulator (pb,sn)te: Surface states and their spin polarization, *Phys. Rev. B* **88**, 045305 (2013).

- [8] C.-Z. Chang, J. Zhang, X. Feng, J. Shen, Z. Zhang, M. Guo, K. Li, Y. Ou, P. Wei, L.-L. Wang, Z.-Q. Ji, Y. Feng, S. Ji, X. Chen, J. Jia, X. Dai, Z. Fang, S.-C. Zhang, K. He, Y. Wang, L. Lu, X.-C. Ma, and Q.-K. Xue, Experimental observation of the quantum anomalous hall effect in a magnetic topological insulator, *Science* **340**, 167 (2013).
- [9] F. Wang, H. Zhang, J. Jiang, Y.-F. Zhao, J. Yu, W. Liu, D. Li, M. H. W. Chan, J. Sun, Z. Zhang, and C.-Z. Chang, Chromium-induced ferromagnetism with perpendicular anisotropy in topological crystalline insulator sntc(111) thin films, *Phys. Rev. B* **97**, 115414 (2018).
- [10] T. Story, R. R. Gajzka, R. B. Frankel, and P. A. Wolff, Carrier-Concentration-Induced Ferromagnetism in Pbsnmtc, *Phys. Rev. Lett.* **56**, 777 (1986).
- [11] B. A. Assaf, F. Katmis, P. Wei, C.-Z. Chang, B. Satpati, J. S. Moodera, and D. Heiman, Inducing magnetism onto the surface of a topological crystalline insulator, *Phys. Rev. B* **91**, 195310 (2015).
- [12] M. A. Ruderman and C. Kittel, Indirect exchange coupling of nuclear magnetic moments by conduction electrons, *Phys. Rev.* **96**, 99 (1954).
- [13] H. Imamura, P. Bruno, and Y. Utsumi, Twisted exchange interaction between localized spins embedded in a one- or two-dimensional electron gas with rashba spin-orbit coupling, *Phys. Rev. B* **69**, 121303(R) (2004).
- [14] M. Sherafati and S. Satpathy, Rkky interaction in graphene from the lattice green's function, *Phys. Rev. B* **83**, 165425 (2011).
- [15] M. Sherafati and S. Satpathy, Analytical expression for the rkky interaction in doped graphene, *Phys. Rev. B* **84**, 125416 (2011).
- [16] M. Shiranzai, H. Cheraghchi, and F. Parhizgar, Effect of the rashba splitting on the rkky interaction in topological-insulator thin films, *Phys. Rev. B* **96**, 024413 (2017).
- [17] H.-R. Chang, J. Zhou, S.-X. Wang, W.-Y. Shan, and D. Xiao, Rkky interaction of magnetic impurities in dirac and weyl semimetals, *Phys. Rev. B* **92**, 241103(R) (2015).
- [18] M. V. Hosseini and M. Askari, Ruderman-kittel-kasuya-yosida interaction in weyl semimetals, *Phys. Rev. B* **92**, 224435 (2015).
- [19] D. Mastrogiuseppe, N. Sandler, and S. E. Ulloa, Hybridization and anisotropy in the exchange interaction in three-dimensional dirac semimetals, *Phys. Rev. B* **93**, 094433 (2016).
- [20] V. Kaladzhyan, A. A. Zyuzin, and P. Simon, Rkky interaction on the surface of three-dimensional dirac semimetals, *Phys. Rev. B* **99**, 165302 (2019).
- [21] L. Fu, Topological Crystalline Insulators, *Phys. Rev. Lett.* **106**, 106802 (2011).
- [22] S.-Y. Xu, C. Liu, N. Alidoust, M. Neupane, D. Qian, I. Belopolski, J. D. Denlinger, Y. J. Wang, H. Lin, L. A. Wray, G. Landolt, B. Slomski, J. H. Dil, A. Marcinkova, E. Morosan, Q. Gibson, R. Sankar, F. C. Chou, R. J. Cava, A. Bansil, and M. Z. Hasan, Observation of a topological crystalline insulator phase and topological phase transition in pb_{1-x}sn_xte, *Nature Commun.* **3**, 1192 (2012).
- [23] P. Dziawa, B. J. Kowalski, K. Dybko, R. Buczko, A. Szczerbakow, M. Szot, E. Lusakowska, T. Balasubramanian, B. M. Wojek, M. H. Berntsen, O. Tjernberg, and T. Story, Topological crystalline insulator states in pb_{1-x}sn_xse, *Nature Mater.* **11**, 1023 (2012).
- [24] J. Liu, W. Duan, and L. Fu, Two types of surface states in topological crystalline insulators, *Phys. Rev. B* **88**, 241303(R) (2013).
- [25] C. M. Polley, P. Dziawa, A. Reszka, A. Szczerbakow, R. Minikayev, J. Z. Domagala, S. Safaei, P. Kacman, R. Buczko, J. Adell, M. H. Berntsen, B. M. Wojek, O. Tjernberg, B. J. Kowalski, T. Story, and T. Balasubramanian, Observation of topological crystalline insulator surface states on (111)-oriented pb_{1-x}sn_xse films, *Phys. Rev. B* **89**, 075317 (2014).
- [26] R.-J. Slager, A. Mesaros, V. Juricic, and J. Zaanen, The space group classification of topological band-insulators, *Nature Phys.* **9**, 98 (2013).
- [27] C.-K. Chiu, H. Yao, and S. Ryu, Classification of topological insulators and superconductors in the presence of reflection symmetry, *Phys. Rev. B* **88**, 075142 (2013).
- [28] T. Morimoto and A. Furusaki, Topological classification with additional symmetries from clifford algebras, *Phys. Rev. B* **88**, 125129 (2013).
- [29] P. Jadaun, D. Xiao, Q. Niu, and S. K. Banerjee, Topological classification of crystalline insulators with space group symmetry, *Phys. Rev. B* **88**, 085110 (2013).
- [30] W. A. Benalcazar, Jeffrey C. Y. Teo, and T. L. Hughes, Classification of two-dimensional topological crystalline superconductors and majorana bound states at disclinations, *Phys. Rev. B* **89**, 224503 (2014).
- [31] C. Fang and L. Fu, New classes of three-dimensional topological crystalline insulators: Nonsymmorphic and magnetic, *Phys. Rev. B* **91**, 161105(R) (2015).
- [32] M. Diez, D. I. Pikulin, I. C. Fulga, and J. Tworzydło, Extended topological group structure due to average reflection symmetry, *New J. Phys.* **17**, 043014 (2015).
- [33] M. Kargarian and G. A. Fiete, Topological Crystalline Insulators in Transition Metal Oxides, *Phys. Rev. Lett.* **110**, 156403 (2013).
- [34] E. O. Wrasse and T. M. Schmidt, Prediction of two-dimensional topological crystalline insulator in pbse monolayer, *Nano Lett.* **14**, 5717 (2014).
- [35] X. Zhou, C.-H. Hsu, T.-R. Chang, H.-J. Tien, Q. Ma, P. Jarillo-Herrero, N. Gedik, A. Bansil, V. M. Pereira, S.-Y. Xu, H. Lin, and L. Fu, Topological crystalline insulator states in the ca₂As family, *Phys. Rev. B* **98**, 241104(R) (2018).
- [36] T. Morimoto, A. Furusaki, and C. Mudry, Anderson localization and the topology of classifying spaces, *Phys. Rev. B* **91**, 235111 (2015).
- [37] Y. Okada, M. Serbyn, H. Lin, D. Walkup, W. Zhou, C. Dhital, M. Neupane, S. Xu, Y. J. Wang, R. Sankar, F. Chou, A. Bansil, M. Z. Hasan, S. D. Wilson, L. Fu, and V. Madhavan, Observation of dirac node formation and mass acquisition in a topological crystalline insulator, *Science* **341**, 1496 (2013).
- [38] G. D. Mahan, *Many Particle Physics* (Plenum Press, New York, 1993).
- [39] G. Grosso and G. P. Parravicini, *Solid State Physics* (Academic Press, New York, 2014).
- [40] C. Fang, M. J. Gilbert, S.-Y. Xu, B. A. Bernevig, and M. Z. Hasan, Theory of quasiparticle interference in mirror-symmetric two-dimensional systems and its application to surface states of topological crystalline insulators, *Phys. Rev. B* **88**, 125141 (2013).
- [41] M. Shiranzai, J. Fransson, H. Cheraghchi, and F. Parhizgar, Nonlinear spin susceptibility in topological insulators, *Phys. Rev. B* **97**, 180402(R) (2018).

- [42] S. Reja, H. A. Fertig, L. Brey, and S. Zhang, Surface magnetism in topological crystalline insulators, *Phys. Rev. B* **96**, 201111(R) (2017).
- [43] X. Xiao, Y. Liu, and W. Wen, Ruderman–kittel–kasuya–yosida interaction in silicene, *J. Phys.: Condens. Matter* **26**, 266001 (2014).
- [44] F. Parhizgar, H. Rostami, and R. Asgari, Indirect exchange interaction between magnetic adatoms in monolayer mos_2 , *Phys. Rev. B* **87**, 125401 (2013).
- [45] Datta. S., *Electronic Transport in Mesoscopic Systems* (Cambridge University Press, Cambridge, 1995).
- [46] E. McCann and V. I. Fal’ko, Landau-Level Degeneracy and Quantum Hall Effect in a Graphite Bilayer, *Phys. Rev. Lett.* **96**, 086805 (2006).
- [47] F. Adinehvand and H. Cheraghchi, Effect of asymmetric fermi velocity on trigonally warped spectrum of bilayer graphene, *J. Phys. Chem. Solids* **107**, 118 (2017).
- [48] J. J. Sakurai, *Modern Quantum Mechanics* (Cambridge University Press, Cambridge, 1985).
- [49] C. Bena and G. Montambaux, Remarks on the tight-binding model of graphene, *New J. Phys.* **11**, 095003 (2009).
- [50] M. Abramowitz and I. A. Stegun, *Handbook of Mathematical Functions with Formulas, Graphs, and Mathematical Tables* (National Bureau of Standards, Washington, DC, 1972).
- [51] J.-J. Zhu, D.-X. Yao, S.-C. Zhang, and K. Chang, Electrically Controllable Surface Magnetism on the Surface of Topological Insulators, *Phys. Rev. Lett.* **106**, 097201 (2011).
- [52] D. A. Abanin and D. A. Pesin, Ordering of Magnetic Impurities and Tunable Electronic Properties of Topological Insulators, *Phys. Rev. Lett.* **106**, 136802 (2011).
- [53] A. A. Zyuzin and D. Loss, Rkky interaction on surfaces of topological insulators with superconducting proximity effect, *Phys. Rev. B* **90**, 125443 (2014).
- [54] D. K. Efimkin and V. Galitski, Self-consistent theory of ferromagnetism on the surface of a topological insulator, *Phys. Rev. B* **89**, 115431 (2014).
- [55] Y.-W. Lee and Y.-L. Lee, Electrical control and interaction effects of the rkky interaction in helical liquids, *Phys. Rev. B* **91**, 214431 (2015).
- [56] Q. Liu, C.-X. Liu, C. Xu, X.-L. Qi, and S.-C. Zhang, Magnetic Impurities on the Surface of a Topological Insulator, *Phys. Rev. Lett.* **102**, 156603 (2009).
- [57] A. M. Black-Schaffer, Rkky coupling in graphene, *Phys. Rev. B* **81**, 205416 (2010).
- [58] O. Madelung, U. Rössler, and M. Schulz, *Tin telluride (SnTe) crystal structure, lattice parameters: Datasheet from Landolt-Börnstein - Group III Condensed Matter* (Springer-Verlag, Berlin, 1998).
- [59] O. Roslyak, G. Gumbs, and D. Huang, Gap-modulated doping effects on indirect exchange interaction between magnetic impurities in graphene, *J. Appl. Phys.* **113**, 123702 (2013).
- [60] E. Kogan, Rkky interaction in gapped or doped graphene, *Graphene* **2**, 8 (2013).
- [61] Y.L. Luke, *The Special Functions and Their Approximations* (Elsevier Science, Amsterdam, 1969).
- [62] J. L. Fields, The asymptotic expansion of the meijer g-function, *Mathe. Comput.* **26**, 757 (1972).
- [63] M. Inoue, K. Ishii, and H. Yagi, Ferromagnetic ordering in mn-doped snTe crystals, *J. Phys. Soc. Jpn.* **43**, 903 (1977).
- [64] A. Prinz, G. Brunthaler, Y. Ueta, G. Springholz, G. Bauer, G. Grabecki, and T. Dietl, Electron localization in $n - \text{pb}_{1-x}\text{eu}_x\text{Te}$, *Phys. Rev. B* **59**, 12983 (1999).
- [65] M. Inoue, H. Yagi, K. Ishii, and T. Tatsukawa, Electrical resistivity of mn-doped snTe crystals at low temperature, *J. Low Temp. Phys.* **23**, 785 (1976).